The Europa Clipper Gravity and Radio Science Investigation

Erwan Mazarico[1] · Dustin Buccino[2] · Julie Castillo-Rogez[2] ·
Andrew J. Dombard[3] · Antonio Genova[4] · Hauke Hussmann[5] ·
Walter S. Kiefer[6] · Jonathan I. Lunine[7] · William B. McKinnon[8] ·
Francis Nimmo[9] · Ryan S. Park[2] · James H. Roberts[10] · Dipak K. Srinivasan[10] ·
Gregor Steinbrügge[2] · Paolo Tortora[11] · Paul Withers[12]

Abstract

The primary objective of the Europa Clipper mission is to assess the habitability of Europa, an overarching goal that rests on improving our understanding of Europa's interior structure, composition, and geologic activity. Here we describe the Gravity and Radio Science (G/RS) investigation. The primary measurement, the gravitational tidal Love number k_2, will be an independent diagnostic of the presence of a global subsurface ocean, but G/RS will make a number of other key measurements related to Europa's deep interior, silicate mantle-ocean interface, ice shell, ionosphere, and plasma environment. Although radio science is common to many missions, Europa Clipper's orbit and spacecraft configuration during flybys present special challenges for the design of this experiment. The information obtained through G/RS will be complementary to the measurements by the other instruments onboard Europa Clipper, and their combined analysis will refine the geophysical understanding of Europa necessary to best assess its potential habitability.

1 Introduction

The Galilean moon Europa has been the subject of intense scientific interest since the Voyager flybys due to its presumed subsurface ocean and young ice shell (Pappalardo et al. 2009). Its astrobiological potential through the interaction, over billions of years, of this ocean with the silicate interior thrust it to the top of the list of bodies warranting dedicated exploration. The first "ocean world," it has now been joined by other planetary objects known or thought to have had or still harbor liquid water. The combination of long-lived tidal heating, water, and many elements necessary for prebiotic chemistry makes Europa an excellent laboratory for a habitability-focused mission.

Europa Clipper: A Mission to Explore Ocean World Habitability
Edited by Haje Korth, Bonnie J. Buratti and David Senske

Extended author information available on the last page of the article

Europa Clipper is NASA's flagship mission to explore Europa in order to investigate its habitability. The mission has broad science objectives and themes related to its ice shell and ocean, its composition, its geology, and its potential recent activity. These will elucidate Europa's present structure, processes, and interactions with its environment, as well as its evolutionary path. These lessons can then be applied to a much larger set of planetary bodies, both in our Solar System and beyond, and thus contribute to refining the expectations for their habitability.

This manuscript introduces the observations and measurement objectives of the Gravity and Radio Science (G/RS) investigation, one of the ten instruments or investigations of Europa Clipper. This type of experiment is perhaps the most common among planetary probes, as it makes use of the essential spacecraft telecommunication subsystem to collect data. G/RS will contribute unique scientific measurements, and their combination with all the observations made by the Europa Clipper payload will support the overarching mission goals.

Gravity science relies on observing how the spacecraft trajectory deviates from predictions and how physical models, for example of the gravity field due to a layered interior, can be modified to conform to these observations. The primary G/RS objective is to measure the tidal Love number k_2, which describes the gravitational response of Europa to the tidal forcing of Jupiter along its orbit. This number will provide evidence for a global subsurface ocean independent of the magnetic field observations or radar sounding. Other important geophysical parameters can be determined from the same observations, such as static gravity field and orientation, and they will set further constraints on Europa's interior, from ice shell properties to the ocean density to the silicate interior's thermal state. Along with the complementary measurements by the other instruments, these results will support comprehensive interior structure modeling.

How Europa interacts with its environment can also be addressed by the observed frequency shift of the spacecraft radio signal. This *radio science* can inform the structure of Europa's tenuous ionosphere and support the study of Europa's interaction with the Jupiter system environment.

We first present the observations relevant to G/RS that Europa Clipper will make during its flybys of Europa (Sect. 2). We describe the instrumentation, both on the spacecraft and on the ground, necessary to carry these out, as well as the sensitivity particular to a multiple-flyby tour. We introduce the theoretical underpinnings and methodology for the analysis of these observations that will turn them into scientific measurements, and we show the uncertainties that can be expected for these geophysical parameters. In Sect. 3, we detail the geophysical parameters and scientific measurements that can then be addressed regarding Europa's internal structure, from the ice shell, to the ocean, to the rocky interior, as well as Europa's orbital interactions with the other Galilean satellites. In Sect. 4, we discuss the plasma interactions of its ionosphere with the Jupiter magnetosphere.

These measurements and science objectives are of course closely interlinked with the measurements and goals of other Europa Clipper instruments. While some of these connections will be made clear here, we refer the reader to the other manuscripts in this Special Collection, and in particular Roberts et al. (this collection) focused on the interior of Europa.

2 Observations and Methods

In this section, we describe how the G/RS science measurements are derived from the radio observations. As illustrated in Fig. 1, the spacecraft communicates with radio antennas on
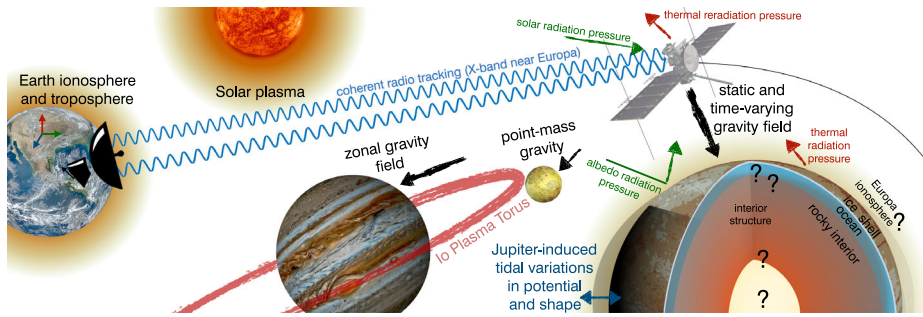
Fig. 1 Illustration of the G/RS experiment geometry. Sizes and locations are notional. The forces acting on the spacecraft are shown with arrows (black for gravitational forces, green for short-wave radiation pressure, red for infrared radiation pressure). Europa's response to tidal forcing by Jupiter modifies its shape and gravity field (dark blue). The radio link (blue) is affected by media effects (troposphere, ionosphere, and plasma). Plasma effects from the Sun and the Io torus only occur on some flybys. Physical parameters related to the interior of Europa and its ionosphere are the focus of the G/RS investigation (question marks)

Earth. The received signal frequency is affected by a number of perturbations that need to be taken into account to infer the contributions of Europa's physical parameters of interest. These include accelerations that the spacecraft experiences and that affect its apparent velocity (e.g., gravity and tidal forces, radiation pressure), as well as delays due to interactions with the environment (e.g., ionosphere, plasma).

2.1 Observational Techniques

2.1.1 Radiometric Tracking

The Gravity/Radio Science investigation utilizes the telecommunications signal between the Earth-based observing stations of NASA's Deep Space Network (DSN, the ground element) and the Europa Clipper spacecraft (the flight element). The Doppler shift of the frequency of the radio signal measures the along-line-of-sight (LOS) motion of the spacecraft, perturbations to its acceleration, and propagation effects.

Radio tracking for the Europa Clipper G/RS investigation will be done in a *coherent* mode, where all radio signals are measured and referenced to the highly stable hydrogen maser frequency reference provided by the DSN (Lauf et al. 2005). A coherent link is established by first transmitting an X-band signal (∼8 GHz) from the DSN to the Europa Clipper spacecraft. The spacecraft's radio receives the signal, multiplies its frequency by a turnaround ratio, amplifies it, and phase-coherently retransmits it back to the DSN for reception. Although the onboard Frontier Radio and RF system (see below) are capable of downlinking at Ka-band frequencies, this capability is not planned to be used during Europa encounters due to geometric constraints (at close range to Europa, the spacecraft will maintain a nadir-pointing attitude for the instrument deck).

This coherent X-band uplink, X-band downlink radio link is typical in deep space tracking applications. Recent examples include the Dawn Gravity Science Investigation at Vesta and Ceres (Konopliv et al. 2011), the InSight Rotation and Interior Structure Experiment on Mars (Folkner et al. 2018), the MAVEN Radio Occultation Science Experiment (Withers et al. 2020), and one of the two links of the Juno Gravity Science Investigation (Asmar et al. 2017). Galileo's radio science instrumentation was designed as a dual S-band and X-band radio system equipped with an Ultra Stable Oscillator (USO). However, after Galileo's high

gain antenna failed to deploy, the spacecraft was limited to S-band communication only through the low-gain antennas (Meltzer 2007). Despite this failure, many of the objectives of the radio science propagation experiments (Howard et al. 1992) and gravitational and celestial mechanics investigations (Anderson et al. 1992) were accomplished.

2.1.2 Radio Occultations

Gravity science measurements close to Europa have the greatest value for revealing Europa's interior structure (Kliore et al. 2004; Verma and Margot 2018). However, the observed received radio frequency in these proximal measurements is also affected by the propagation of the radio signal through Europa's ionosphere (Kliore et al. 1997). The measurement of electron densities in Europa's ionosphere is needed to account for ionospheric effects in the analysis and interpretation of gravity science measurements. They will also support the analysis of induced magnetic field measurements, which are integral to the determination of the thicknesses of Europa's ice shell and subsurface ocean (Kivelson et al. 1997, 1999, 2000; Khurana et al. 1998, 2002; Kivelson et al., this collection) and which are also affected by the conducting ionosphere (Schilling et al. 2004; Saur et al. 2010). The spatial distribution of plasma in Europa's ionosphere illuminates how the magnetosphere creates ions as energetic magnetospheric charged particles impact atmospheric neutrals. It also reveals how the magnetosphere removes ions by stripping them away (Saur et al. 1998; McGrath et al. 2009). In addition, it places constraints on the roles of solar radiation and magnetospheric plasma in creating and processing Europa's atmosphere and surface materials.

Radio occultations are a common method for making remote sensing measurements of vertical profiles of ionospheric electron density at Solar System objects (e.g., Phinney and Anderson 1968; Fjeldbo et al. 1971; Yakovlev 2002; Kliore et al. 2004; Withers 2010). In such observations, a radio signal is sent from a transmitter to a receiver at a time when the ray path between transmitter and receiver passes through the ionosphere and atmosphere of a target object. The radio frequency received at the ground station is affected by refraction in the ionosphere of the target object, leading to a "frequency residual" between observed and predicted values.

Galileo acquired ten electron density profiles at Europa (Kliore et al. 1997; McGrath et al. 2009). On average, the electron density N decreases from near-surface values $\sim$ 9×10^3 cm^{-3} with an exponential scale height H$\sim$240 km (Kliore et al. 1997). Plasma in Europa's ionosphere is thought to be produced from the neutral atmosphere by impact ionization by magnetospheric charged particles and/or solar photoionization, and then lost by flow away from Europa down the magnetospheric wake (Saur et al. 1998; McGrath et al. 2004, 2009).

The ten Galileo profiles are generally consistent with the hypothesis that electron densities are depleted in the magnetospheric wake region and enhanced on the magnetospheric flanks, but they are not sufficient to fully test this hypothesis. Notable spatial and temporal variations in the atmosphere and ionosphere have been seen (Cassidy et al. 2007; McGrath et al. 2004, 2009; McGrath and Sparks 2017). Yet these are hard to explain if the magnetosphere controls source and sink processes for the atmosphere and ionosphere (Cassidy et al. 2007; McGrath and Sparks 2017). Several observations have recently suggested that Europa has plumes (e.g., Roth et al. 2014; Sparks et al. 2017; Jia et al. 2018; Paganini et al. 2019). If plumes are the main source of Europa's ionosphere and atmosphere, they may explain the observed variations. Several of these plume detections occurred years apart above a surface thermal anomaly near Pwyll Crater (25° S, 89° E), which suggests that plumes may be active at a given location for decades (e.g., Roth et al. 2014; Sparks et al. 2017; Jia et al. 2018).

Table 1 Europa Clipper radio frequency links used for gravity and radio science

Link Configuration (uplink/downlink)	Polarization (up-link/downlink)	Uplink Frequency (MHz)	Downlink Frequency (MHz)	Turnaround Ratio
X/X	RCP[a]/RCP	7170	8424.5	880/749
X/Ka	RCP/RCP or RCP/LCP[b]	7170	31860	3328/749

[a]Right-Circularly Polarized

[b]Left-Circularly Polarized

On the other hand, no changes in albedo or color have been detected at this site or others on Europa over the 28 years covered by available Voyager, Galileo, and New Horizons images (Schenk 2020).

Radio occultations have been used to determine the shapes and sizes of solar system objects (e.g., Perry et al. 2015; Hinson et al. 2017). However, the G/RS investigation does not plan to do so for Europa. Instead, Europa Clipper will measure the shape and size of Europa using EIS images, REASON altimetry, and Europa-UVS stellar occultations (Abrahams et al. 2021).

2.1.3 Europa Clipper Specifics

2.1.3.1 Telecom Subsystem and Deep Space Network

Flight Element

Frontier Radio – The Johns Hopkins Applied Physics Laboratory (APL) Frontier Radio lies at the heart of Europa Clipper's telecommunications system (Srinivasan et al. 2017). It is a software-defined radio, in which some components traditionally incorporated as hardware are implemented in software instead. It provides the primary interface between the spacecraft's Command and Data Handling system and the DSN. The Frontier Radio on Europa Clipper is configured with five hardware slices: an X-band receiver slice, an X-band exciter slice, a Ka-band exciter slice, a digital signal processor slice, and a power converter slice. The Frontier Radio provides the necessary stability for precision radio science signals with an instrumental Allan deviation stability of $< 2.3 \times 10^{-13}$ s/s at 60-second count time and a ranging delay of < 66 ns.[1] The radio is configured to DSN Channel 21 X-band and Ka-band. The link configuration of Europa Clipper's telecommunications system is specified in Table 1.

Amplifier – A total of four Traveling Wave Tube Amplifiers (TWTA) provide radio frequency amplification for the downlink. The system consists of two redundant X-band TWTAs operating at a power output of 20 W and two redundant Ka-band TWTAs operating at power output of 35 W.

Antennas – The Europa Clipper spacecraft is designed with a fixed X/Ka-band High Gain Antenna (HGA) and X-band Medium Gain Antenna (MGA) pointed in the spacecraft −Y

---

[1]Europa Clipper Telecommunications Design Control Document, Jet Propulsion Laboratory Internal Document D-101604, Revision A, 22 October 2020.
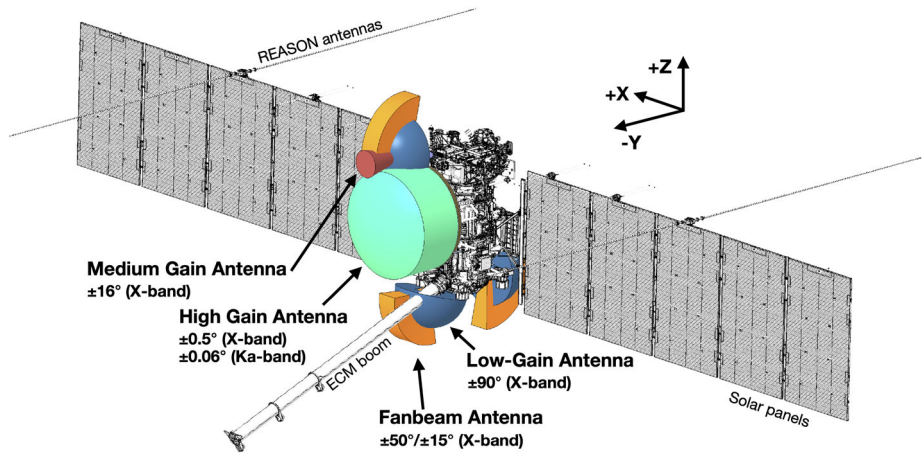
Fig. 2 Europa Clipper spacecraft antenna locations and fields of view

Table 2 Europa Clipper antenna parameters

Antenna	Transmit Boresight Gain (dBi)	Usable Beamwidth (deg)	Antenna Mounting Direction	Antenna Mount Location (mm)
HGA	46 (X-band)	±0.5 (X-band)	−Y	(0, 0, 0)
	57.5 (Ka-band)	±0.06 (Ka-band)		
MGA	17.9	±16	−Y	(0, −314, −560)
LGA1	6	±90	+Y	(−454, 0, −513)
LGA2	6	±90	−Y	(−349, −229, −197)
LGA3	6	±90	−Z	(0, 0, -283)
FBA1	12	±90 (wide)	−Y/+Z	(390, −409, 50)
		±15 (narrow)		
FBA2	12	±90 (wide)	−Y/−Z	(−939, −495, 856)
		±15 (narrow)		
FBA3	12	±90 (wide)	+Y/−Z	(−1083, 505, 610)
		±15 (narrow)		

direction (Fig. 2). Science instruments are mounted on the +Y deck; during Europa encounters the spacecraft will point the +Y axis nadir to the surface of Europa. Thus, typical tracking with the HGA will not be possible during Europa flybys. Instead, three X-band Fanbeam Antennas (FBAs) are included to allow for carrier-only Doppler tracking during Europa encounters. FBAs have a wide beam axis and a narrow beam axis. The three FBAs are mounted in the Y/Z plane with the narrow beam axis along the X direction. Additionally, there are three X-band Low Gain Antennas (LGAs) with symmetric beam patterns mounted in the +Y, −Y and −Z directions. The −Z direction LGA is placed on the spacecraft for initial acquisition during launch and is not designed to be used at Jupiter distances. Table 2 shows the gain, beamwidth, and placement of the antennas onboard the Clipper spacecraft.

The operation and performance of this system configuration will be unlike previous missions due to a combination of a large Earth-Jupiter distance and prime data collection with FBAs and LGAs. Due to the nadir pointing of the spacecraft $+Y$ axis, a typical encounter with Europa will involve sweeping through large portions of the beam pattern of multiple antennas. Furthermore, the use of the lower-gain FBAs and LGAs will result in low downlink signal-to-noise ratios. Results from previous deep space tracking and ground testing suggest that a threshold of 4 dB-Hz is sufficient for open-loop tracking, below the typical closed-loop tracking threshold of 10 dB-Hz with 1 Hz bandwidth (O'Dea and Kinman 2019).

Ground Element

Deep Space Network – The Deep Space Network is a set of large-aperture antennas placed strategically in complexes at Goldstone, California; Madrid, Spain; and Canberra, Australia, to provide near-constant communications with spacecraft in the Solar System. Each complex consists of one 70-meter diameter station, and several 34-meter diameter stations. Each station has an exciter-transmitter system to provide uplink support and microwave subsystem in the front-end, which provides low-noise amplification and first stage down-conversion. At X-band, this is a High Electron Mobility Transistor (HEMT). A fixed down-conversion is applied from 8.1 GHz to 300 MHz intermediate frequency (IF) for distribution to the back-end closed-loop and open-loop receivers. A Frequency and Timing System (FTS) located at each complex provides a reference frequency and clock synchronization among all equipment using a hydrogen maser.

Closed-Loop Doppler Tracking – The DSN's Block V Closed-Loop Receivers (BVR) are a part of the Downlink Tracking and Telemetry Subsystem (DTT). An additional down-conversion is applied to bring the IF signal to a frequency range representing the expected range of received frequencies. The Receiver, Ranging, and Telemetry (RRT) processor acquires and tracks the incoming carrier signal with a phase-locked loop. The downlink carrier phase is measured by the phase-locked loop at a 0.1-second interval. The observed frequency is then calculated as the difference of two phase values divided by the time between the phase measurements (Moyer 2000).

Open-Loop Recording – The DSN's Open-Loop Receivers (OLR) provide a method to capture the entire spectrum of the received signal and record it for later processing. The OLRs digitize and down-convert the IF signal by a downlink frequency prediction to near baseband. The raw antenna voltage samples at baseband are then saved as In-phase and Quadrature (IQ) samples at a given sampling rate. For narrow-band radio science measurements, the sampling rate is typically between 1 kHz and 100 kHz. Because the signal is not tracked by the OLRs in real-time, the IQ samples must be post-processed to yield the Doppler observables for the Gravity/Radio Science investigation. Several post-processing algorithms have been developed for radio science analysis, including Fast Fourier Transforms (FFTs), spectral optimization of FFTs (Paik and Asmar 2010), Doppler-rate compensated FFTs (Buccino et al. 2020), and a phase-locked loop (Buccino et al. 2018). Traditionally, phase-locked loops are used for gravity science investigations as they provide the most precise Doppler observables and are not limited by the bin size of the FFT.

Noise Budget & Requirements

Noise sources in deep space tracking are well understood (e.g., Asmar et al. 2005). Such noise sources include thermal noise, instrumentation noise (frequency and timing noise, oscillator noise, antenna mechanical noise), and propagation noise (Earth troposphere, Earth

Table 3   Noise budget for Europa Clipper G/RS Doppler measurements

Noise source (in mm/s)	Predicted noise contribution	Potential noise contribution	Explanation
Thermal	0.0211	0.0084 – 0.0267	Eq. (2) with $P_c/N_0 = 4$ dB-Hz and $B_L = 0.25$ Hz at 60-second integration time. Will decrease when P_c/N_0 rises above 4 dB-Hz threshold
Solar Plasma	0.0698	0.0298 – 0.0783	Sun-Earth-Probe angle of 30° at 60-second integration time (O'Dea and Kinman 2019), decreases significantly as Sun-Earth-Probe angle increases to ∼90° and then levels off
Troposphere	0.0329	0.0074 – 0.0346	Troposphere scintillation level at 60-second equivalent assuming white frequency noise spectral shape (from Asmar et al. 2005), highly variable with season at tracking site
Frequency Reference & Ground Electronics Noise	0.0075	0.0026 – 0.0075	DSN radio science requirement 3×10^{-14} at 100 sec (Rogstad 2020), includes both Frequency and Timing (FTS) and ground electronics contribution, scaled to 60-sec. Measured performance is superior (Asmar et al. 2005)
DSN Antenna Mechanical Noise	0.010		60-second equivalent assuming white phase noise spectral shape (from Asmar et al. 2005)
Spacecraft Electronics	0.0345		Predicted performance of Frontier radio (Allan deviation 2.3×10^{-13} at 60 sec)
Total	0.0878	0.048 - 0.0969	Root-sum square of noise components

ionosphere, plasma noise). Of particular importance to the Europa Clipper G/RS investigation are plasma noise and thermal noise. A sample noise budget is shown in Table 3.

The primary sources of plasma noise between Earth and the Europa Clipper spacecraft at Jupiter are from the solar plasma and the Io Plasma Torus. Solar plasma noise increases as the radio path gets closer to the Sun, which occurs during a superior solar conjunction. Earth-Jupiter superior solar conjunctions will occur on 31 October 2029, 01 December 2030, 01 January 2032, and 03 February 2033, causing an increase in noise around those dates for any tour trajectory. O'Dea and Kinman (2019) modeled the solar plasma noise as a function of the Sun-Earth-Probe (SEP) angle. For an SEP angle of 30°, the noise contribution from solar plasma is 0.0698 mm/s (two-way) and SEP angle of 3° is 1.108 mm/s. The Io Plasma Torus is a region of particles trapped in Jupiter's magnetosphere approximately around the orbit of Io. When the radio signal propagates through the torus, the signal experiences a phase delay from the electrons along the line of sight (Phipps and Withers 2017).

Instrumental noise sources occur on both the DSN and the spacecraft sides. The random noise introduced by radio components is typically white phase noise from either clock noise or instability in the individual RF components. DSN instrumental noise is quantified through the DSN requirement (Rogstad 2020) or measurements (Asmar et al. 2005). The spacecraft's instrumental noise is estimated from the stability requirement of the Frontier radio (2.3×10^{-13} at 60-second integration time), to be measured on the ground during telecom development. Allan deviation is converted to standard deviation under the white phase

Table 4 Europa Clipper G/RS Tracking requirements

Name	Requirement
Gravity Science Dataset Telecom Antenna Configuration	When collecting Doppler dataset measurements, the DSN/spacecraft link shall support a 2-way coherent Doppler measurement with a received *Pt/No* level > 4 dB-Hz, when the Earth is in the antenna field of view of the spacecraft.
Precision for Gravity Science Velocity Tracking	When collecting gravity science dataset measurements, the Project System shall generate Doppler radiometric data to an accuracy of 0.1 mm/s (1-sigma) for a 60 s count time when the Sun-Earth-Probe angle > 27°, and to an accuracy of 5 mm/s when the Sun-Earth-Probe angle is greater than 3° and less than 27°

noise assumption ($\sigma = f_c \sigma_y$, where f_c is the carrier frequency from Table 1 and σ_y is the Allan deviation).

Thermal noise is contributed from the fact that there is a finite signal-to-noise ratio in the link. The error contribution to the Doppler from thermal noise in units of velocity can be expressed as (assuming negligible uplink thermal noise; adapted from O'Dea and Kinman 2019):

$$\sigma_V = \frac{2}{2 f_c} \frac{\sqrt{2 B_L}}{2\pi T_c / N_c},$$ (1)

where c is the speed of light, f_c is the downlink carrier frequency, B_L is the loop bandwidth, T_c is the integration time, and P_c/N_0 is the downlink signal-to-noise ratio. This formulation assumes that the uplink signal-to-noise ratio is much larger than the downlink signal-to-noise ratio. In order for the phase-locked loop to track the signal, a loop signal-to-noise ratio (the carrier signal-to-noise ratio divided by the loop bandwidth) of >7-10 dB-Hz is desired. With a minimum signal-to-noise ratio of 4 dB-Hz the corresponding required loop bandwidth should be 0.4 Hz; then the thermal noise contribution to Doppler will be 0.0267 mm/s. Thus, at most SEP angles, the dominant noise source is solar plasma but thermal noise is not insignificant. With the narrow loop bandwidth required, the signal residual Doppler rate and Doppler acceleration must be low enough such that the static phase error does not cause a loss of lock. Open-loop data is flexible and allows for reprocessing of the recorded signal; for example, a phase model can be used to drive the phase-lock loop such that a lower loop bandwidth can be used (e.g., Buccino et al. 2018).

From this noise budget, two requirements are established for G/RS, one for a minimum signal-to-noise level and one for Doppler tracking precision (Table 4).

2.1.3.2 Tour Trajectory and Europa Coverage The Europa flyby tour is designed to achieve good spatial coverage through repeated, streamlined encounter activities. Unlike the Galileo and Cassini missions, the flybys of the other Galilean moons are purely designed to support this Europa-focused tour. The two phases of Europa flybys are distinguished by the observed hemisphere: about two dozen mostly sub-Jovian flybys followed by roughly the same number of mostly anti-Jovian flybys. Each phase is preceded by a months-long transition period that leverages flybys of Ganymede and Callisto. This strategy maximizes the number of flybys and the robustness of the tour, and fulfills the instrument observation requirements. High-latitude flybys are particularly important to distinguish the gravitational flattening and
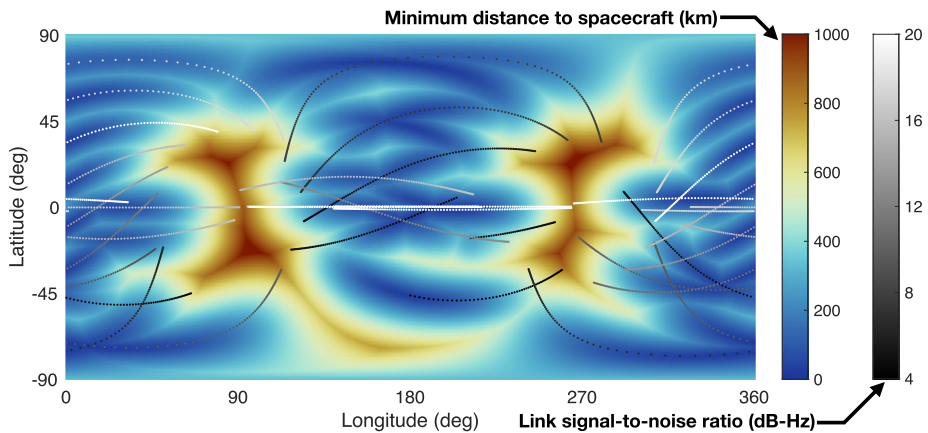
Fig. 3 Minimum distance achieved by Europa Clipper to the surface of Europa (shown in color). Ground-tracks are shown for altitudes less than 1500 km when link is sufficient for radio contact (gray values indicate signal-to-noise ratio Pt/No). The 19F23 trajectory is shown here, which is representative of the coverage expected for the tours under consideration

ellipticity of Europa, which are important geophysical parameters that inform knowledge of the interior structure. Nevertheless, two regions near the equator on the leading and trailing hemispheres are not observed at low altitudes. While global-scale features can be readily observed, such as Europa's tidal response, this coverage has implications for the resolution of shorter-scale features.

Figure 3 shows the minimum distance between the spacecraft and the surface after all flybys. This example is obtained with the 19F23 trajectory,[2] but the broad features remain consistent with other tour options. Given that the sensitivity to gravitational features is directly related to distance, the two low-latitude regions near 90° E and 270° E with larger sampling distances will be resolved more coarsely compared with the majority of Europa. This also limits the overall resolution of the gravity field, as an unobserved region precludes robust determination of all gravity field coefficients at resolutions better than its size (Sect. 3.1.3).

Another constraint deriving from the flyby trajectory is placed on the ability to actually acquire the Doppler observations necessary to observe Europa's gravity figure. Besides occultations by Europa, the strength of the radio link between the ground stations and the spacecraft is especially challenging. As described in Sect. 2.1.3.1, the LGAs and FBAs have limited gain compared to the HGA, but the nadir-ram spacecraft orientation near Europa constrains the path of the Earth in the spacecraft frame, and thus prescribes the gain that can be expected by any antenna. The timing of each flyby also sets the Earth-Jupiter distance, which affects the link. Figure 4 shows the resulting coverage in the ±2 hours tracking periods around closest approach for the 19F23 flybys; most flybys can be tracked with a sufficient radio link but several cannot be observed. This is significantly better than in early development phases of Europa Clipper, where the minimum link threshold assumption was higher than 4 dB-Hz, and thus prevented tracking on many flybys (10 dB-Hz for Solomon et al. 2016; 7 dB-Hz for Verma and Margot 2018).

---

[2]Available at the NAIF website: https://naif.jpl.nasa.gov/pub/naif/EUROPACLIPPER/.
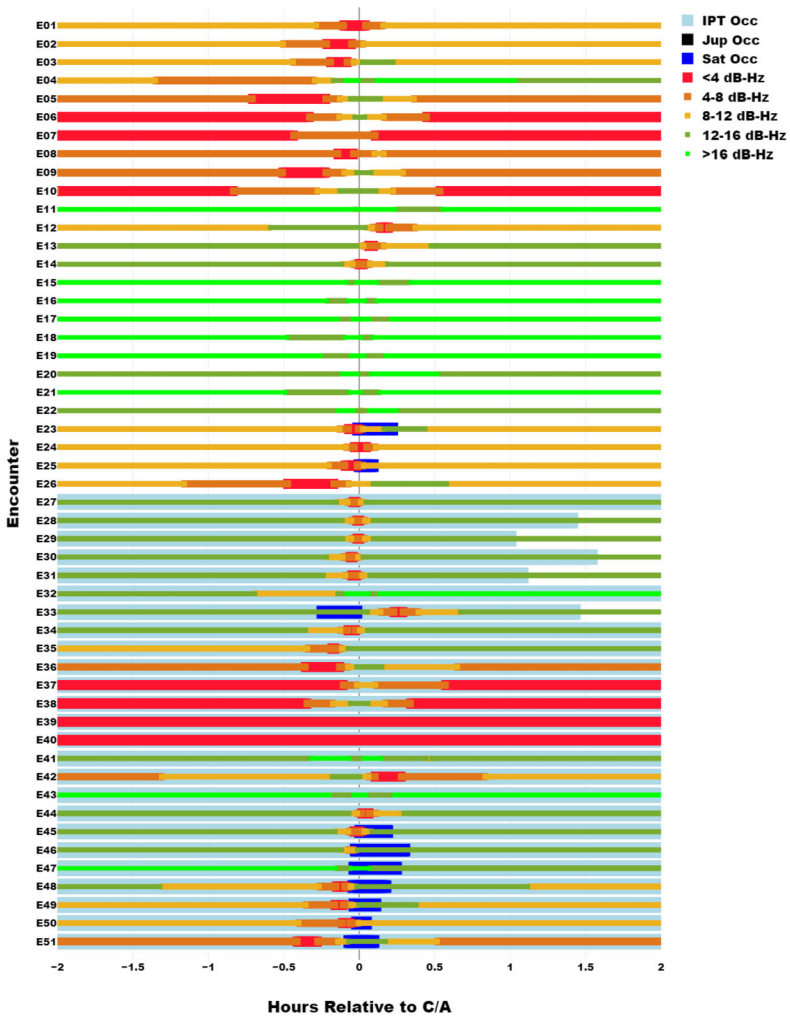
Fig. 4 Summary of the radio tracking coverage of Europa Clipper in the ±2-hour window around each closest approach (C/A). The 19F23 tour is shown as an example. The power-to-noise ratio (*Pt/No*) is binned; values < 4 dB-Hz (red) are not expected to be sufficient for producing Doppler observations

2.2 Methods

2.2.1 Gravity Science

2.2.1.1 Orbit Determination The radiometric data of the Clipper spacecraft will be processed and filtered using Orbit Determination (OD) software, such as Mission Analysis, Operations, and Navigation Toolkit Environment (MONTE) and GEODYN.

MONTE is a high-precision orbit determination software developed at the Jet Propulsion Laboratory for planetary navigation and gravity science based on over 50 years of similar experience (Evans et al. 2018). MONTE employs a least-squares approach to converge orbital arcs and is capable of processing DSN Doppler, range, and imaging data. MONTE has

been used to determine the gravity field and rotational parameters of numerous planetary bodies, including Vesta (Konopliv et al. 2014), Ceres (Konopliv et al. 2018), Jupiter and its moons (Folkner et al. 2017; Iess et al. 2018; Durante et al. 2020; Gomez Casajus et al. 2021), Saturn and its moons (Iess et al. 2012, 2014; Tortora et al. 2016; Iess et al. 2019; Durante et al. 2019; Zannoni et al. 2020; Lainey et al. 2020), and Mars (Konopliv et al. 2016), and will be used to navigate the Europa Clipper spacecraft as well.

GEODYN II is an orbit determination and geodetic parameter estimation software developed and maintained at the Goddard Space Flight Center (Pavlis and Nicholas 2017). It is based on batched least squares estimation (Montenbruck and Gill 2000; Tapley et al. 2004). It has been used for several decades for Earth and planetary geodesy analysis of many varied measurement types. It was used to process the radiometric data of numerous planetary orbiters, from the Moon (Apollo, Clementine, Lunar Prospector, Lunar Reconnaissance Orbiter, GRAIL; Lemoine et al. 1997; Mazarico et al. 2009; Lemoine et al. 2013; Goossens et al. 2017, 2021; Mazarico et al. 2018) to Mars (Lemoine et al. 1997; Genova et al. 2016) to Mercury (Mazarico et al. 2014; Genova et al. 2019) to icy satellites (van Noort et al. 2020) and small bodies (Goossens et al. 2021). It was used to jointly process radiometric data with altimetry and imagery datasets, similarly to what can be expected for Europa Clipper, with LRO and OSIRIS-REx in particular (Mazarico et al. 2018; Goossens et al. 2021).

At the end of the OD process, the reconstructed spacecraft trajectory and an updated set of force and measurement model parameters is obtained. The remaining misfits between the observed and computed Doppler measurements, called Doppler residuals, may still contain scientifically valuable information, in particular related to short-scale gravity features, which are small compared with the overall (global) gravity field resolution. Other estimation techniques beyond OD can recover geophysical insights from these LOS spacecraft velocity residuals.

2.2.1.2 Force Models To integrate the spacecraft trajectory, each force affecting the spacecraft needs to be accounted for. The accuracy of the models of these forces is important to ensure that the physical parameters can be estimated without bias and directly relate to physical signals.

The gravitational forces from major planetary bodies including the Jupiter system moons are modeled as point-mass interactions, except from Jupiter and Europa. As is common, these objects are modeled under the spherical harmonics formalism (Kaula 1966; Heiskanen and Moritz 1967). The gravitational potential of a body is expressed as a spherical harmonics series and can be evaluated at a point (longitude φ, latitude λ, radius r) outside the body's reference radius R_e with the expression:

$$U = \frac{GM}{r} + \frac{GM}{r} \sum_{l=2}^{\infty} \sum_{m=0}^{l} \left(\frac{R_e}{r} \right)^l P_{lm}(\sin\lambda) \cdot (C_{lm}\cos(m\varphi) + S_{lm}\sin(m\varphi)) \qquad (2)$$

where G is the gravitational constant, and M is the body mass. The product GM is also called the gravitational parameter, and is what can be directly estimated through geodetic measurements. P_{lm} is the 4π-normalized associated Legendre polynomial of degree l and order m, which are directly related to the wavelength (resolution) of the field features described by the corresponding C_{lm} and S_{lm} coefficients, also called the normalized Stokes coefficients. The values of these gravity field coefficients are primarily constrained by Juno for Jupiter (e.g., Durante et al. 2020) and by Galileo and Juno for Europa (Anderson et al. 1998; Gomez Casajus et al. 2021). The Jupiter gravity field is primarily zonal (order $m = 0$) and known to degree $l = 15$ ($\sim$14,000 km wavelength). Europa's field is not well known;

our current knowledge is limited to the longest-wavelength (gravitational ellipticity, C_{22}). The gravitational accelerations are the gradients of this potential and can be evaluated with similar but more complex expressions (Kaula 1966).

In addition to the static gravity field, Europa Clipper will sense the time-variable gravity field of Europa, itself the result (response) of the tidal forcing by Jupiter (and to a much lesser extent the Sun and the other Galilean satellites). The tidal Love number k_2 relates these:

$$U_{\text{tide}} = k_2 \, U_{\text{forcing}} \tag{3}$$

The tidal acceleration on the spacecraft can be similarly computed from the gradient of U_{tide}. Alternatively, the tidal contribution to Europa's total field can be accounted for through corrections to the C_{lm} and S_{lm} coefficients (Kaula 1966; Park et al. 2015), which also allows the estimation of several tidal Love numbers per degree (k_{20}, k_{21}, k_{22}), which have different spatio-temporal sensitivities. However, our simulations show that the Europa Clipper Doppler data would not allow an independent estimation of k_{20}, k_{21}, and k_{22}. With the Europa Clipper tour trajectory, the k_{22} parameter is much better determined than the other. We constrain the k_{20}, k_{21}, and k_{22} values to be equal and thus obtain a single k_2 estimate, fully observable with a small formal uncertainty (see Sect. 2.3).

Other perturbations are much smaller in magnitude. Due to their non-conservative nature unlike the gravity acceleration, these so-called non-gravitational forces are important to model accurately. Partial or incorrect modeling will result in signatures in the tracking data residuals that may lead to biases and increased errors during the parameter inversion. For instance, a systematic mismodeling of solar radiation pressure may alias into the estimated gravity field, i.e., an offset in some C_{lm} and S_{lm} coefficients may partially accommodate the same perturbations, or degrade the precision of their determination.

The solar radiation pressure acceleration can be modeled with various methods and fidelity. While a constant cross-section ("cannonball") may be sufficient for simulation efforts, data analysis requires realistic evaluation. Simple box-wing shape models with 10 to 20 plates, with prescribed area and specular and diffuse reflectivities, have typically been used to compute the spacecraft cross-section in the Sun's direction and the resulting acceleration (Marshall and Luthcke 1994; Konopliv et al. 2006, 2013; Lemoine et al. 2013). Self-shadowing between plates has been considered, particularly with asymmetric spacecraft shapes (Konopliv et al. 2006; Mazarico et al. 2009). Higher-fidelity modeling by ray-tracing millions of rays that interact with a complex spacecraft shape model has been used in Earth geodesy (Ziebart 2001; Li et al. 2018) and recently for planetary missions (e.g., Leonard et al. 2019; Goossens et al. 2021).

In proximity of Europa, additional accelerations are imparted both by the sunlight reflected off Europa's surface and by its thermal infrared emission. These planetary albedo and thermal radiation pressure accelerations are more complex to model as they originate from extended sources, with varying apparent intensity (irradiance) and to which the spacecraft offers a range of cross-sections. Maps of albedo and thermal emission will be refined by Europa Clipper measurements (from EIS and E-THEMIS in particular; see Turtle et al. and Christensen et al. in this collection) and may be incorporated in for modeling although their effect on the G/RS analysis is anticipated to be very small.

The spacecraft thermal re-radiation acceleration can be modeled from telemetered temperature data or a thermal model of the spacecraft. Antenna recoil acceleration can be simply computed based on antenna field of view and power transmitted (e.g., Geeraert et al. 2019).

If plumes are observed by Europa Clipper (Daubar et al., this collection), plume density models could be used to compute the expected drag acceleration and to evaluate their consistency with the radio tracking data. Indeed, drag forces needed to be considered in the

analysis of Cassini tracking data for both Titan's atmosphere (Iess et al. 2012; Durante et al. 2019) and the Enceladus plumes (Iess et al. 2014).

2.2.1.3 Measurement Models Each radio tracking measurement needs to be computed quantitatively before comparison with the observed value. Knowledge of the spacecraft trajectory is a dominant contributor to the computed observations, but additional corrections need to be considered to achieve the level of accuracy required by the science objectives. So-called measurement models are used to account for these effects.

Radiometric measurements depend on the inertial positions of the antenna phase centers of both spacecraft and station. The knowledge of the spacecraft antenna phase center in the spacecraft frame relies on pre-launch antenna characterization and surveys. To obtain its inertial position, it first needs to be translated relative to the location of its center of mass (CoM). The CoM position in the spacecraft frame changes after each propulsive event, when propellant is used and changes the overall mass distribution; it will be reconstructed by the Guidance, Navigation, and Control (GN&C) team. Uncalibrated errors in the antenna offset would generate apparent Doppler shifts due to centrifugal forces. The inertial orientation is derived from precise telemetered attitude information. The positions of the ground stations and their antenna phase centers are known precisely from surveys, but temporal variations and drifts from the effects of tidal deformation, ocean loading on the crust, and plate tectonics need to be applied (e.g., IERS-International Earth Rotation and Reference Systems Service; Petit and Luzum 2010).

The single coherent link in X-band will be affected by several noise sources including Earth's wet troposphere and ionosphere, solar plasma, Europa's ionosphere, and the Io Plasma Torus (IPT). The media corrections due to the Earth atmosphere and ionosphere are obtained from calibration data acquired at the DSN stations. Mapping functions are applied to translate zenith delays to the correct elevation (e.g., VMF, Boehm and Schuh 2004). Earth's wet troposphere undergoes seasonal variations at the DSN station, and its calibration is particularly important in the Ka band. The total electron content (TEC) of Earth's ionosphere is measured globally at hourly timescales using global positioning system dual-frequency links (Lanyi and Roth 1988); uncalibrated ionospheric effects should be negligible. An additional media effect is the IPT that is formed by ionized particles trapped into Jupiter's magnetic field lines in a toroidal shape. The propagation of the radio signal through this dispersive medium causes Doppler shifts. To mitigate the IPT effects, theoretical and semi-empirical models will be used to at least partially compensate for frequency shifts induced by the plasma. Another major perturbation during superior solar conjunctions is caused by the solar corona (Iess et al. 2014). Because of Earth-Jupiter relative geometry, the radio tracking data of Europa will be significantly perturbed by solar plasma only during a few flybys of Europa; given the highly variable nature of the solar plasma, models for corrections are not available and the expectation is that the effective data noise level will be increased.

2.2.1.4 Other Europa Clipper Tracking Observations The radio tracking measurements collected by the DSN are critical to the gravity investigation. Collected during every flyby in a ± 2 h window around closest approach, they result in a good spatial coverage, nearly uniform at scales >400 km (Fig. 3). The multiple-flyby tour, tracked by radio, provides good observability of some key geophysical parameters (e.g., C_{20}, k_2). However, other geodetic datasets obtained by the Europa Clipper payload can complement their sensitivity to the spacecraft trajectory and support the estimation of additional geophysical parameters. In this section, we briefly describe how joint estimation or constraints obtained from other investigations can complement the G/RS science objectives.

Radio tracking alone is not sensitive to the radial surface deformation from tides, i.e., to the tidal Love number h_2 which relates to the body tide amplitude (expected to be approximately ±30 m for a h_2 of $\sim$1.2; Moore and Schubert 2000). In contrast, the radar signals transmitted by REASON interact directly with the surface, and can thus constrain the range to the surface. While h_2 is strongly correlated with k_2, a combination of both tidal Love numbers significantly increases the information that can be obtained on the interior structure of Europa (see Roberts et al., this collection). Similar to the use of laser altimetry crossovers to measure the body tide (Mazarico et al. 2014; Steinbrügge et al. 2015; Hussmann et al. 2018; Thor et al. 2021; Bertone et al. 2021), the overlapping REASON coverage at the intersection of two groundtracks obtained at two tidal phases (i.e., at two positions in Europa's orbit) can constrain the relative elevation change due to tidal deformation (Steinbrügge et al. 2018). Unlike laser altimeter data, which is pulse limited as the laser beam is focused on a footprint of usually few tens of meters, the radar illuminates a larger area of the surface. As a consequence the analysis of the radar returns relies on topographic data around each crossover point from the EIS Wide-Angle Camera (WAC; see Turtle et al., this collection) to exploit the ambiguity of the radar returns and obtain multiple statistically independent range measurements. This analysis requires sufficient signal strength (altitude $\lesssim$1000 km) in which case the measurement precision is dependent mostly on the surface roughness properties (Steinbrügge et al. 2020) but is expected to be $\sim$5-10 m. The analysis also needs to account for the trajectory reconstruction errors, which a joint inversion of the radio tracking data and REASON crossovers would naturally provide, and for an a priori estimate of the Digital Terrain Model (DTM) location with respect to the radar footprint. The number of usable crossovers depends on the location and temporal distribution of the groundtracks, typically 100 to 200 depending on the considered trajectory tour. These differential measurements can provide a measurement of h_2 with a formal precision of $\sim$0.1 ($\sim$8%). A specific characteristic for the incorporation into the joint inversion is that the individual surface ranges gained by this method are strictly speaking only a range from the spacecraft to the DTM, which may initially have an inaccurate geodetic position. However, since the same DTM is used for the two profiles (flybys) of a crossover point, the ambiguity in radial positioning of the DTM cancels out when computing the differential range (Steinbrügge et al. 2018). Considering the differential ranges at crossover points in a joint inversion with radio science observations brings an additional set of independent and complementary observables. The network of globally distributed intersections ties individual tracks together and therefore imposes additional geodetic consistency and accuracy to the orbit solution. A joint inversion can therefore improve the orbit position knowledge and would subsequently enhance the determination of gravity parameters as well.

The imaging data collected by EIS could also be used to improve the estimates of Europa's tidal Love numbers (h_2 and k_2), gravity field, and rotational parameters (Park et al. 2011, 2015, 2020). Similar to radar altimetry, repeat images of the same longitude and latitude points (i.e., crossover points) would be needed to create control points and triangulate the spacecraft position; the improvement in orbit accuracy would then contribute to the accuracy of recovered gravity and rotational parameters. The importance of EIS data for gravity science mainly depends on the reconstructed knowledge of camera pointing, imaging geometry in general and especially of crossover points (distance, solar illumination angles, etc.), and the number and frequency of crossover point observations (e.g., sampled over different values of Europa's true anomaly for measuring its tidal variation). It is also possible that EIS will be able to detect periodic lateral (east and north) displacements of the ice shell, which are controlled by the third Love number l_2 (Ermakov et al. 2021). Measuring l_2 would provide additional constraints on the mechanical properties of the ice shell, but to do so would require careful disambiguation from other periodic motion (e.g., librations).

G/RS constraints on the thickness of the ice shell, and density of the ocean and rocky core are complementary to other types of measurements to be done by Europa Clipper. Shell thickness can influence the abundance and intensity of potential hot spots associated with the underlying ocean, and which may be detected by E-THEMIS (Christensen et al., this collection). The presence of extruded ocean material at the surface – salts, organics – should also be related to shell thickness, and the concentration of salts in localized surface deposits informs the ocean composition. Mapping of these materials spectroscopically by MISE (Blaney et al., this collection) and direct sampling of such non-ice compounds by SUDA (Kempf et al., this collection) and MASPEX (Burch et al., this collection) will quantify the relationship between the crustal geophysical parameters and extrusion of oceanic material. Different types of geologic features are expected to correlate with shell thickness, ranging from cycloidal fractures in thin shells to preservation of crater topography in thicker shells. The EIS instrument (Turtle et al., this collection) will image such features at an unprecedented level of detail that will allow the mechanisms of feature formation to be fully quantified. Details on measurements by each of these instruments is given in the respective chapters as well as the composition chapter.

2.2.2 Line-of-Sight Analysis

The Doppler shift recorded during tracking can be converted to spacecraft velocity in the line-of-sight (LOS), and thence into line-of-sight acceleration. These LOS accelerations can be used to derive a spherical harmonic map of global surface gravity (see above). However, doing so usually requires suppression of short-wavelength signals, as they are otherwise amplified during the downwards continuation process. An alternative is to use the LOS accelerations directly, so that all the short-wavelength information is retained.

The full procedure for doing so is given in the case of Magellan data by McKenzie and Nimmo (1997), and applications to Europa are described in James (2016) and Roberts et al. (2018). The basic idea is that the surface topography can be used to predict the expected LOS acceleration of the spacecraft. By comparing the expected acceleration to that observed as a function of wavelength, the admittance (ratio of gravity to topography) can be recovered. This admittance will contain information about the compensation state and mechanical properties of the ice shell (Sect. 3.1.3.2). The great advantage of the LOS admittance technique is that the short wavelengths, which are less subject to interference by mantle gravity anomalies, are not discarded.

2.2.3 Occultations

Europa Clipper will conduct radio occultation observations of the ionosphere of Europa during flybys and other opportunities. Radio occultation observations will be conducted in a two-way configuration using a range of spacecraft antennas. The DSN transmits an uplink, carrier-only signal at X-band to Europa Clipper. The spacecraft receives this signal and coherently retransmits downlink, carrier-only signals at X-band to multiple antennas at the DSN complex. Each receiving DSN antenna records the incoming signal at kHz sampling rates on an open loop receiver. As on Cassini, the uplink signal's frequency is steered so that coherent lock is re-established rapidly on egress (Schinder et al. 2015). This technique will permit egress occultation observations to extend as near to the surface as possible. For example, at Titan, coherent lock was re-established by Cassini within 1 km of the surface. Operationally, the planned radio occultations during flybys impose no additional requirements beyond those associated with tracking for gravity science purposes.

Fig. 5 Recovery of tidal Love number k_2 during a typical tour trajectory (19F23)
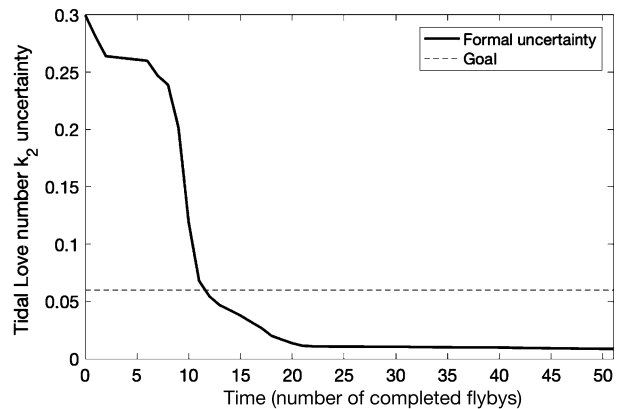
After the occultation is complete, DSN and JPL radio science support staff generate a time series of the received downlink frequency at the desired time resolution. They also predict the expected value of the received frequency using the relativistic Doppler shift between transmitter and receiver. Analysis of the time series of the frequency residuals, defined as observed minus expected received frequency, yields a vertical profile of electron density around Europa.

2.3 Simulations

Before the OD software can be used to analyze the actual radio tracking data collected during the Europa campaign flybys, they can support simulation efforts to ascertain the expected recovery uncertainties for the various geophysical parameters of interest. Simulations with both software packages, MONTE and GEODYN, were conducted within the scope of the Europa Clipper project, by the Europa Gravity Science Working Group in 2015-16 (Solomon et al. 2016), subject matter experts during Phase B (Verma and Margot 2018), and after their selection by G/RS team members. Here, we report the formal uncertainties of recent simulations performed with the 19F23 tour trajectory (Buffington et al. 2019). These covariance analysis simulations will be followed in later mission phases by more comprehensive simulations where the initial state is perturbed, but they provide valuable information into the capabilities of Europa Clipper's G/RS investigation.

The tracking data coverage is based on realistic mission planning and DSN scheduling, as well as visibility constraints related to occultations and link (power-to-noise $Pt/No > 4$ dB-Hz). The simulations assume a 0.1 mm/s noise at 60 s integration time but also account for degraded performance at low SEP angles due to solar plasma. In addition to the spacecraft initial state, a solar radiation scale factor and additional stochastic accelerations are considered to account for mismodeling effects.

Figure 5 shows the evolution of the recovery of the tidal Love number k_2 over the Europa flyby campaign. Even if considering a scaling of the formal uncertainty by a factor of 2 to account for unmodeled systematic effects (Solomon et al. 2016), the retrieval is significantly better than the Level-1 science requirement of 0.06.

Table 5 shows the range of parameter uncertainties for k_2, low-degree gravity coefficients C_{20} and C_{22}, and the pole position (right ascension and declination at the J2000 epoch) and obliquity. The formal uncertainties of the geophysical parameters of interest obtained by previous studies through the analysis of Galileo radio tracking data (Anderson et al. 1998;

Fig. 6 Power spectra of the simulated Europa gravity field (black) and of the recovered gravity field uncertainty at the end of the 19F23 tour (blue)
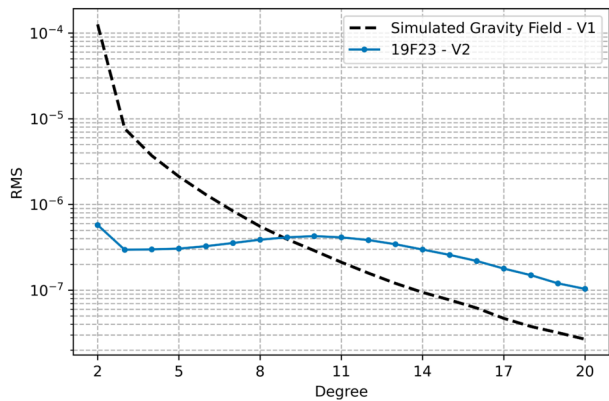
Table 5 Recovered formal uncertainties for key geophysical parameters. An additional scale factor of 2-3 is typically used to obtain more realistic 1-σ uncertainties to be used in the science analysis. References: [1] Jacobson et al. (2000); [2] Gomez Casajus et al. (2021); [3] Davies and Katayama (1981); [4] Bills et al. (2009); [5] Rhoden et al. (2010)

Parameter	Current/Expected value	Uncertainty, Current knowledge	Uncertainty, Europa Clipper
k_2	0.2-0.3	-	$1.4\text{-}1.8 \times 10^{-2}$
C_{20}	$4000\text{-}5000 \times 10^{-7}$	800×10^{-7} [1,2]	$3.5\text{-}8.5 \times 10^{-7}$
C_{22}	$1250\text{-}1400 \times 10^{-7}$	$20\text{-}25 \times 10^{-7}$ [1,2]	$1.5\text{-}2.3 \times 10^{-7}$
Pole Right Ascension	268.08°	$\sim$0.27° [3]	0.08-0.20°
Pole Declination	64.51°	$\sim$0.07° [3]	0.04-0.08°
Obliquity	0.1-1.5° [4,5]	-	0.04-0.08°

Jacobson et al. 2000; Gomez Casajus et al. 2021) are compared to the expected results from Europa Clipper gravity simulations. The exact tour choice will impact the G/RS investigation results, but we expect the simulations conducted with future tour candidates such as 19F23 to be representative. Indeed, the 21F31 tour baseline, which is current as of the time of this writing, shares many similarities. These parameters and associated scientific insights will be further discussed in Sect. 3.

Figure 6 shows the power spectrum of the recovered gravity field. A Kaula-type $1/l^2$ regularization is applied during inversion; because the rocky interior dominates the low-degree power, an additional radial attenuation normalizing factor is imposed, to account for the total hydrosphere depth (Pauer et al. 2010; Park et al. 2015). The assumed, or anticipated, gravity field power is closely tied to the recovered resolution, that is the spherical harmonics degree at which the signal-to-noise ratio (SNR) becomes less than unity. In a low-power case (e.g., deeper ocean), the global field can be measured only up to $l \sim 8$, while in more favorable high-power cases, one could resolve the gravity up to $l > 10$. The decrease of the formal uncertainties at $l > 10$ is due to the use of the Kaula constraint, as it serves to limit the gravity field power at higher degrees where the tracking data do not provide sufficient information.

The uncertainties of the degree-2 coefficients (C_{20}, C_{22}, S_{22}) are notably lower than previously expected (Verma and Margot 2018), in part because of the change in tour trajectory and tracking coverage, but primarily because of a change in the estimation procedure. Here, only the time-variable tidal potential is allowed to contribute to the estimation of the tidal Love number k_2. While this does not affect the k_2 uncertainty itself, it significantly reduces the correlations between k_2 and the degree-2 gravity coefficients, leading to uncertainties $\ll 10 \times 10^{-7}$ on C_{20} and C_{22} (Table 5). Without this correction to the partial derivatives (excluding the permanent tide term), the C_{20} and C_{22} uncertainties increase to 20-25 $\times 10^{-7}$ and 30-40 $\times 10^{-7}$, respectively, values consistent with the $\sim 30 \times 10^{-7}$ and 50×10^{-7} values of Verma and Margot (2018).

In these simulations, the spin rate of Europa was not estimated. Without a precise measurement from other methods (such as a control network of EIS images over the mission duration), its estimation from radio tracking alone would weaken the solution, because of high correlations with some degree-2 gravity coefficients (which are related to the principal axes frame), and would result in higher uncertainties (deterioration by a factor of 5 or more). This would directly impact the knowledge of the moment of inertia and thus the ability to determine the interior structure. The estimated spin rate precision from EIS observations is $\sim 3 \times 10^{-6}$ deg/day (see Turtle et al., this collection), which is marginally sufficient to decorrelate the rotation rate from the gravity coefficients (the correlation of k_2 with libration is low, <0.2).

3 Geophysical Parameters

This section describes how the geophysical parameters to be obtained by Europa Clipper following the methodology just outlined contribute to a better understanding of Europa's internal structure. The primary objective of the G/RS investigation is the measurement of k_2 in order to confirm the subsurface ocean, but the other independent parameters will enable the broad examination of Europa's structure down to its deep interior.
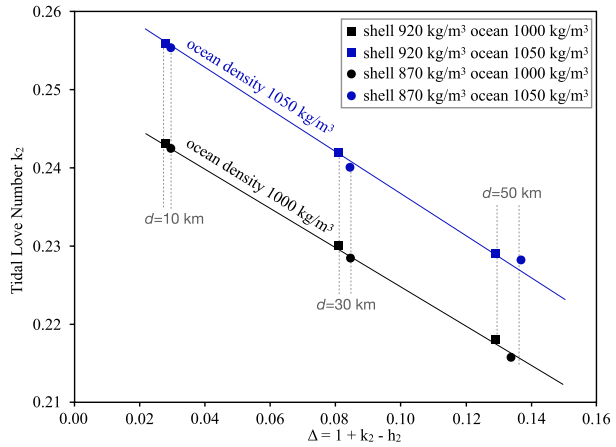
3.1 Ice Shell

3.1.1 Tidal Love Number k_2

The tidal response of a body to an external perturbing potential is described by the so-called tidal Love numbers, k_2 and h_2, where the subscript denotes the spherical harmonic degree. The quantity k_2 is defined as the ratio of the induced potential change to the perturbing tidal potential. A uniform, strengthless body has a k_2 value of 1.5, but material rigidity or mass concentration towards the center significantly reduces k_2. In the presence of an ocean beneath Europa's ice shell, we expect a k_2 of about 0.23 (see Fig. 7), with a modeled range of $\sim \pm 0.02$, and a phase lag of order 1° or less (Moore and Schubert 2000). Without a global subsurface ocean, k_2 would be reduced to <0.015. A measurement of k_2 with an accuracy of 0.06 is therefore sufficient to distinguish between these two end members. In the case of an ocean, a smaller measurement uncertainty (0.014-0.018, Table 5) can provide one constraint on Europa's shell thickness and rigidity.

The tradeoff between the rigidity and inferred shell thickness, however, represents the biggest difficulty in using k_2 to determine the thickness independently. For instance, a fractured near-surface layer will have a low rigidity compared with coherent, intact ice; less obviously, a convecting layer may have a low effective rigidity, if the ice viscosity is low

Fig. 7 Tidal Love number k_2 and $\Delta = 1 + k_2 - h_2$ for various combinations of shell thickness (d), ocean density, and shell density. Note that deriving d from Δ is not subject to uncertainty due to uncertainties in ocean density. The models assume an elastic mantle of radius 1481 km, density 3310 kg m^{-3} and rigidity 100 GPa overlying a liquid core of radius 874 km and density 4440 kg m^{-3}. Ice rigidity is taken to be 3.3 GPa and the ice shell is elastic

enough. Layers exhibit reduced effective rigidity if the Maxwell time (viscosity/rigidity) is comparable to or less than the forcing period, in this case 3.55 days. In short, k_2 is sensitive to the thickness of the rigid part of the ice shell, which may not be the same as the total shell thickness.

Layers with a low enough viscosity will also give rise to a phase lag between the perturbing potential and the tidal response. This phase lag can also be estimated as the imaginary part of k_2, Im(k_2), where k_2 and rigidity are both treated as complex quantities that affect time variations of different degree-2 gravity coefficients. The rate of tidal heating is directly proportional to Im(k_2). The measurement of Im(k_2) is challenging and needs to be assessed further.

The ocean density is another property introducing ambiguity in the interpretation of k_2 (Fig. 7). That parameter is expected to range between 1000 (pure water) and 1050 kg m^{-3} (saline) or more if one combines the amplitude and phase of the induced magnetic field (Schilling et al. 2007) with an assumed shell thickness $\lesssim$ 40 km (Howell 2021; Castillo-Rogez et al. 2022). In addition, higher pressures alone will increase Europan ocean water densities by several percent over STP values. For a full discussion of possible ocean compositions see Becker et al. (this collection).

3.1.2 Tidal Love Number h_2

While the tidal Love number k_2 describes the induced gravitational field due to a redistribution of mass in the interior, another effect of the gravitational forcing by Jupiter is the deformation of the surface. The amplitude of the radial deformation scales linearly to the amplitude of the tidal potential with the factor h_2/g, where g is the gravitational acceleration at the surface and h_2 the tidal Love number commonly used to describe the radial deformation of the body. Like k_2, h_2 directly depends on the interior of Europa, in particular on the thickness and rheology of the ice shell. If both h_2 and k_2 can be measured, then the ambiguity in shell thickness arising from uncertainties in some other parameters of interest (e.g., ocean density) can be reduced (Wahr et al. 2006). Figure 7 demonstrates this result, showing how $\Delta = 1 + k_2 - h_2$ and k_2 vary with shell thickness d, shell density, and ocean density. Neither k_2 nor Δ are very sensitive to shell density. But for k_2, uncertainty in what ocean density to assume maps into a large uncertainty in shell thickness (Fig. 7). Conversely for Δ, the uncertainty in ocean density has no effect on the inferred shell thickness. Note, however, that h_2 will be determined with less precision than k_2 ($\sim$0.1 as opposed to $\sim$0.015) by

Europa Clipper (Roberts et al., this collection). Furthermore, this approach does not resolve the fundamental tradeoff between shell thickness and rigidity.

As for k_2, dissipation induces a tidal phase lag in the radial deformation. If dissipation mostly occurs in the ice shell, the phase lag is expected to be very similar to the phase lag of k_2 and a measure of the total energy dissipation from tides. However, if dissipation can also occur in the silicate mantle (Běhounková et al. 2020), the h_2 phase lag would be less sensitive to it, and a phase lag difference between k_2 and h_2 would indicate dissipation in the deep interior. For typical silicate viscosities the phase-lag difference would be on the order of 1° or less. However, with the presence of partial melt in the mantle the effective viscosities might be lower which would imply phase-lag differences of up to several degrees (Hussmann et al. 2016).

The measurement of Europa's tidal Love numbers therefore directly contributes to the mission goals of the Europa Clipper mission by investigating the structure of the outer ice shell and the primary energy source of the satellite, in addition to their prime roles in sub-surface ocean detection/confirmation. While inferences from a single Love number and to a lesser extent also the combination of k_2 and h_2 are ambiguous, it is the integration of these parameters into a larger suite of geophysical and other measurements that allows an in-depth characterization of Europa's interior (Roberts et al., this collection).

3.1.3 Static Gravity Field

3.1.3.1 Shell thickness Variations and Tidal Heating In an ice shell, tidal heating is larger at the poles and smaller at the equator (Ojakangas and Stevenson 1989). For a conductive shell, these variations in tidal heating, combined with latitudinal variations in surface temperature, give rise to lateral variations in equilibrium shell thickness. In turn, these variations in shell thickness give rise to surface topography, assuming that the shell is (Airy) isostatically compensated. These topography variations can be quite large, roughly 2 km for a 40 km thick shell (Nimmo et al. 2007). However, if the ice shell is thinner, or the shell is convective, such variations will be reduced or negated, respectively, or possibly reversed. These variations dominantly occur at spherical harmonic degrees 2 and 4; but because the shell is compensated, the resulting long-wavelength gravity anomalies are expected to be small, a few mGal (Fig. 8d). By contrast, the gravity anomalies expected from the degree-2 tidal and rotational distortion are expected to be several hundred mGal (Fig. 8a).

3.1.3.2 Topography and Density Anomalies Within the Ice Shell In addition to the long-wavelength tidal deformation of Europa's ice shell, it is also plausible that shorter-wavelength gravity anomalies are present, similar to those found on Ganymede (Anderson et al. 2004; Palguta et al. 2009). The simplest model for Europa's ice shell assumes a pure, solid water ice density of 920 kg m^{-3}. But compositional variations are likely important, as substantial non-ice components have been detected in Galileo NIMS and Earth-based spectra of stratigraphically and visually darkened and reddened regions (Carlson et al., 2009; Becker et al., this collection). The ice shell is likely variably contaminated with alkali halide and sulfate salts, though to an uncertain degree (Zolotov and Kargel 2009). Examples of these localized density variations could include upwelling diapirs of warm buoyant ice, or pockets or lenses of meltwater or brine (Roberts et al. 2018); these are illustrated in Fig. 9 (Vance et al. 2015). Pappalardo and Barr (2004) and Lesage et al. (2020) suggested impurity densities due to salts and sulfates of up to 1670 kg m^{-3} (epsomite), which would imply a density contrast with respect to water ice of up to 750 kg m^{-3} (though it is not anticipated that a freezing brine body would have so high a density overall). Clathrates have also been
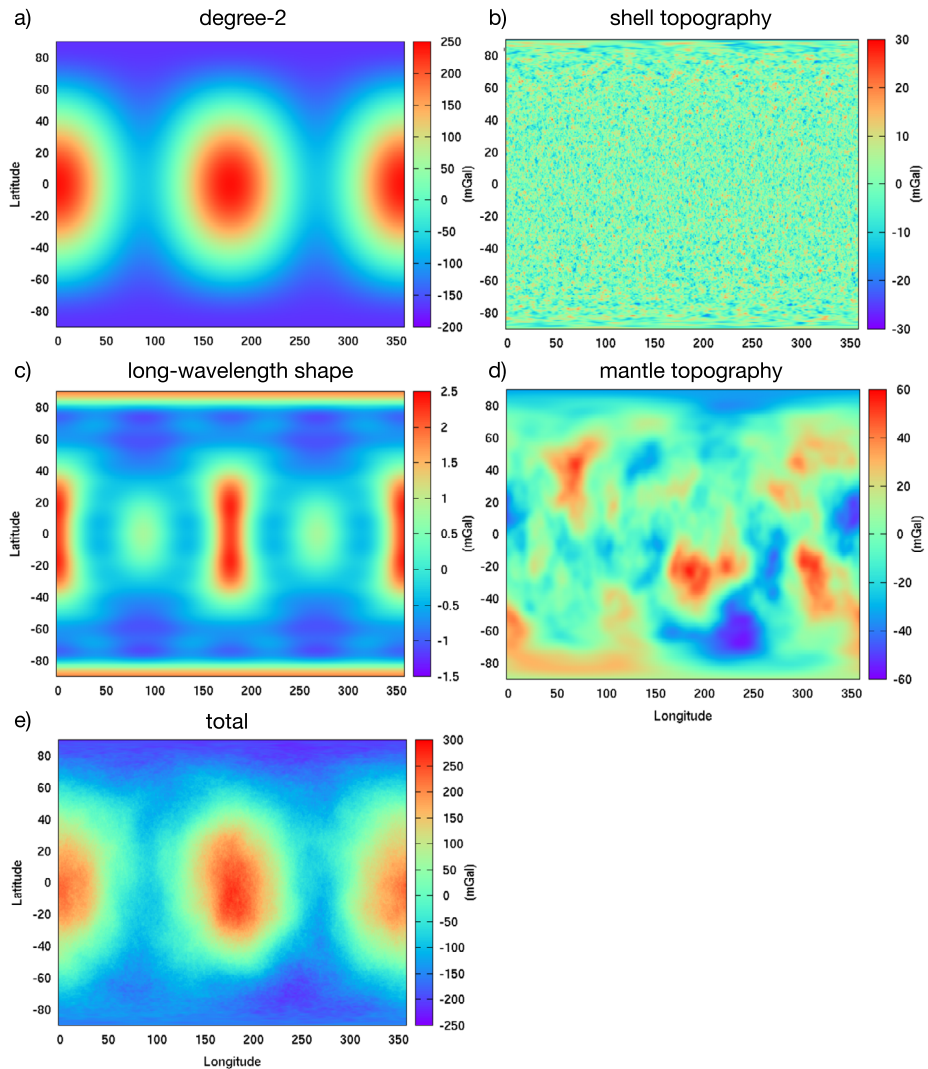
Fig. 8 a) Degree-2 gravity following Anderson et al. (1998). b) Gravity due to shell topography. The surface topography is taken to have a power-law slope of −1 and a peak-to-peak variation of 2 km. The shell is assumed partially compensated with an elastic and shell thickness of 6 km and 20 km, respectively. c) Gravity due to long-wavelength shape variations, after Nimmo et al. (2007). d) Gravity due to mantle topography, which has an assumed power-law slope of −1.8 and peak-to-peak amplitude of 2 km. Note that this topography has been generated randomly and is currently unconstrained by observations. e) Total gravity field. Further details on calculation methods are given in Koh et al. (2022)

proposed, of O_2 principally, but of CO_2 and SO_2 as well, produced radiolytically at Europa's surface and ultimately distributed within the ice shell (Hand et al. 2006).

Lateral variations in ice shell porosity could also contribute to density variations, although differential compaction would not change the total column density. The near-surface of the ice shell may be porous from some combination of impacts and tectonic fracturing. This low-density porous region is expected to extend to no deeper than one-third of the
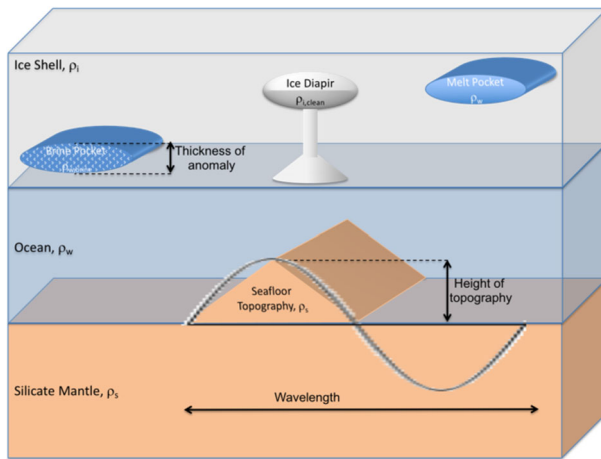
Fig. 9 Examples of structures in Europa's subsurface that may produce gravity anomalies detectable by the Europa Clipper: seamounts at the bottom of the liquid ocean; diapirs, brine pockets, and melt pockets in the solid ice (Adapted from Vance et al. (2015)). The scales of these features as shown in the figure are exaggerated with respect to their actual sizes. Characteristic scales for the features are 10 s of km in width, and < 1 km in height, compared to ice shell and ocean thicknesses on order 10 km and 100 km respectively. Characteristic densities for clean ice diapirs, dirty ice matrix, silicate seafloor, brines and water are 925 kg m^{-3}, 1025 kg m^{-3}, 2700-3500 kg m^{-3}, 1360 kg m^{-3}, and 1000 kg m^{-3}, respectively, although considerable variation would be expected in this values

conductive shell thickness (Nimmo et al. 2003), but could be less if porosity-generating mechanisms are not operating. The potential effects of porosity and compositional/phase variations may, however, be difficult to untangle from gravity measurements alone, as they have opposite effects on ice shell density at the 10% level.

Regardless of these complications, we can estimate the magnitude of the effects expected for Europa Clipper. Assuming a 10 km thick brine layer and $\delta\rho$ of 335 kg m^{-3} (based on densities in the caption for Fig. 9, the resulting gravity anomaly is 12 mGal at 50 km altitude and 2.5 mGal at 200 km assuming flexure of a spherical shell with an elastic lithosphere thickness of 30 km and Young's modulus of 1 GPa. For a 10 km thick lithosphere, the gravity anomaly is 7.7 mGal at 50 km and 1.5 mGal at 200 km. The larger amplitudes in principle would be readily detectable given the expected precision of Europa Clipper gravity observations (Verma and Margot 2018). Separating these anomalies from the contributions of the silicate interior may prove a challenge, however (see next paragraph). Furthermore, Europa Clipper's ability to resolve features at these kinds of wavelengths is limited by the brief time it spends at low altitude during each flyby. As a result, detecting such anomalies is likely to require analysis of the line-of-sight acceleration of individual flybys (James 2016; Roberts et al. 2018; Sect. 2.2.2). The density contrast between the silicates and the ocean is far stronger than any potential density anomalies in the ice shell. The seafloor topography dominates the long-wavelength (> 200 km) gravity signature and is detectable up to 2000 km away from the surface. However, the signal from the seafloor is attenuated through the entire thickness of the ocean and ice shell, and wavelengths shorter than 40 km are not detectable even at closest approach. The short wavelength (< 100 km) gravity is thus dominated by anomalies in the ice shell. However, because of the relatively low density contrast (e.g., between clean and dirty ice, or between ice and meltwater) they are only evident within 100 km of the surface. Additional observations, such as radar sounding would be needed to

resolve inherent ambiguity between the density and thickness of the mass anomaly, and to identify its composition. The trajectory of Europa Clipper affords a unique opportunity to make observations at a variety of distances, which can help to resolve multiple anomalies in the same regions; for example, a seamount and a diapir. The seafloor topography will dominate far away and the anomalies in the ice shell will dominate close up. By analyzing such spectral differences with spacecraft altitude, we can investigate the relative contributions of the seafloor and ice shell mass anomalies (Vance et al. 2015; Roberts et al. 2018).

The limited relief of Europa's short wavelength topography (Nimmo et al. 2003; Schmidt et al. 2011), combined with short horizontal length scales and rapid vertical attenuation, makes gravity anomalies from topography even more difficult to detect in orbital data. The actual magnitude of any anomaly observed by Europa Clipper will depend on how close the spacecraft flies to the center of the anomaly and on the orientation of the line-of-sight vector to Earth.

The amplitude of a given gravity anomaly depends on its density, thickness, and compensation state. Observations made by other Europa Clipper instrument teams can be used to restrict the allowed ranges of some of these parameters, which will sharpen the interpretations of the gravity data and lessen ambiguities. If a gravity anomaly is correlated with a compositionally distinct unit as seen in MISE observations, this connection would suggest that the anomaly is related to an ice sheet structure. The MISE composition results can be used to estimate plausible densities for the structure, which can be used in the gravity modeling to derive the thickness of the mass anomaly. Similarly, REASON or ECM data may provide an independent constraint on ice shell thickness. On the other hand, if there is no compositional anomaly associated with the gravity anomaly, or if the layer thickness required to explain the anomaly exceeds the plausible thickness of the ice shell, these results will be evidence that some or all of the gravity anomaly is related to ocean floor topography (Sect. 3.3.2). In the unlikely event that no gravity anomalies are detected, it would place strong bounds on both the ice shell thickness and on the range of ocean floor topography. This finding would be an important science result in its own right.

The unique trajectory of Europa Clipper provides an opportunity to potentially deconvolve gravity anomalies arising from density variations in the ice shell from those due to seafloor topography. Because the spacecraft is at altitude, mass anomalies within the ice shell will always be closer to the point of observation - and thus less attenuated - than seafloor topography. Seafloor topography, however, has a much greater density contrast than any plausible variation within the ice shell. At long horizontal distances on Europa (>1000 km), the potential field will therefore be dominated by seafloor topography (Pauer et al. 2010, and see Sect. 3.3.2 below). In contrast, density variations within the ice shell should dominate at short wavelengths (<100 km), but may only be evident within 100 km of closest approach (James 2016; Roberts et al. 2018; Koh et al. 2022).

Finally, the admittance (ratio of gravity to topography at a particular wavelength) provides a way of determining the elastic thickness and potentially the density of the ice shell. The admittance increases over a wavelength range determined by the elastic thickness, and then flattens out to a value determined by the surface density. Thus with sufficiently good data, both of these quantities may be determined (e.g., Akiba et al. 2022). In practice, global spherical harmonic models of Europa's gravity will not have sufficiently high spatial resolution to carry out this kind of analysis (Koh et al. 2022), but LOS admittance plots from individual flybys may provide the high spatial resolution required to estimate surface shell density (James 2016; Roberts et al. 2018), especially when combined with topography derived from EIS or REASON.

3.1.4 Librations

From a point on the surface of Europa, Jupiter does not occupy the same position in the sky but wobbles (librates) backwards and forwards. This so-called optical libration occurs because Europa's orbital speed changes, due to its eccentric orbit and the influence of other moons, while its rotation speed is constant, to first order. Jupiter's back-and-forth motion imposes torques on Europa, which causes its rotation rate to vary periodically. These physical librations can generate stresses (Hurford et al. 2009), in addition to those caused by the optical libration and variation in Europa's instantaneous distance from Jupiter. The diurnal libration amplitude also potentially provides information about the interior structure, as the reaction of Europa's ice shell to the external torque depends primarily on the thickness and rigidity of the outer ice shell (Van Hoolst et al. 2013).

A quantitative analysis by Van Hoolst et al. (2013) suggests that in the particular case of Europa, the influence of various poorly known parameters such as ocean density will limit the sensitivity of the internal structure to the amplitude of the diurnal librations (expected to be about 140 m). One should, however, be cautious in concluding that observations of librations would not be useful. In the case of a decoupled shell, the rocky interior and the shell will experience diurnal librations of different amplitudes. Because gravity will be sensitive to the combined effects of these librations, while imaging will see only the shell libration, a combination of gravity and imaging measurements might be able to separate out these two effects and provide interesting constraints on the interior structure. However, the expected uncertainty of the gravity-based libration amplitude measurement is large ($\sim$400 m) and thus unlikely to provide additional constraint under a nominal scenario.

Further, it is important to keep track of long-period librations ($\sim$10 days or greater) for cartographic purposes and for orbit determination because their amplitudes can be large (up to $\sim$1 km; see also Roberts et al., this collection and Bills and Scott 2022).

3.2 Ocean

The Europa ocean salinity is unknown. However, the density of the ocean is expected to be low ($<$1100 kg m^{-3}, ignoring compressibility; Zolotov and Kargel 2009), unless the salt concentration was increased by progressive freezing of the shell over time. The Galileo magnetometer data provide a lower bound on electrical conductivity of 0.5 S/m (for a 100-km-thick ocean under a 25-km-thick ice shell) that is consistent with a salinity of a few tens of g/kg (Hand and Chyba 2007), although an upper bound cannot be derived from available data (Schilling et al. 2007) (see Roberts et al., this collection). A reference shell thickness of $\sim$40 km (Howell 2021) leads to a slightly larger minimum conductivity. It has also been suggested that a thick layer of CO_2 clathrate hydrates could accumulate at the base of Europa's ocean (Melwani Daswani et al. 2021). The density of CO_2 clathrate is up to 1140 kg m^{-3} (Sloan and Koh 2008). In a similar vein, if Europa's silicate interior were to be, or to have been, volcanically active, and if its style of volcanism resembled that of Io, then the ocean floor may also host a layer of sulfur and/or SO_2 clathrate (McKinnon and Zolensky 2003).

This density contrast between ocean and icy shell is too small to generate a resolvable signature in the moment of inertia (Fig. 13). On the other hand, the tidal Love numbers h_2 and k_2 are influenced by the ocean density. The Love number k_2 increases by $\sim$0.013 per +50 kg m^{-3}, all other parameters being equal (e.g., Castillo et al. 2000; Steinbrügge et al. 2018; Fig. 7). This increase is equivalent to a shell thickness change of 20 km ($-$0.013 per +20 km; Fig. 7). This level of precision is near the edge of what can be achieved by

the mission. A measurement of h_2 to the same precision, while challenging, would remove the uncertainty in shell thickness arising from that in the ocean density (Fig. 7). Hence, complementary compositional constraints from the Europa Clipper magnetometer (ECM) and compositional instruments (see Becker et al., this collection), coupled with the gravity data, are critical to the derivation of shell thickness from inversion of k_2.

The knowledge of the gravity field of Europa to degree 10 or above may provide further information on the silicate interior. Indeed, the observed gravity field spectrum can be related via downward continuation to the intrinsic sea floor gravity spectrum given the sea floor radius (or conversely, the hydrosphere thickness; Dombard and Sessa 2019). The induction signal measured by ECM is the primary means for measuring this hydrosphere thickness, and the observed gravity spectrum may then be used to constrain the logarithmic slope of the gravity power spectrum of the silicate interior, which dominates at low degrees ($l <20$, Fig. 11; Pauer et al. 2010). We currently lack any constraint on the silicate interior of Europa, relying on empirical observations at other bodies (Pauer et al. 2010; Ermakov et al. 2018); any observational constraint will thus allow us to put Europa in perspective with the outer surfaces of e.g., the Moon, Earth, and Venus (Koh et al. 2022).

3.3 Silicate Mantle

3.3.1 Hydrostatic Equilibrium

The moment of inertia (MoI) of Europa provides information on the global density profile, and thus the degree of internal differentiation, and may lead to constraints on the hydrosphere thickness when combined with additional (e.g., bulk compositional) information. The mean MoI can be derived from the gravity moments under the Radau-Darwin approximation (RDA) for synchronously rotating moons (e.g., Hubbard 1984; Murray and Dermott 1999; Van Hoolst et al. 2008; Gao and Stevenson 2013). This method provides the equation that ties the mean MoI, I, to the gravity field coefficients J_2 and C_{22}, if the celestial body is hydrostatic (Schubert et al. 2009), that is, if it does not possess any long-term strength. The ice shell is not expected to be rigid enough to depart from a hydrostatic shape at long wavelengths; however, the silicate mantle (and thus the overall gravity) could well be non-hydrostatic, depending on its history and temperature. The Moon, perhaps an analogue to Europa's interior, is very strongly non-hydrostatic (though it is a very slow rotator and not substantially tidally heated, characteristics that permit substantial non-hydrostaticity). Dione was also found to significantly depart from hydrostatic equilibrium (Zannoni et al. 2020). On the other hand, Titan's gravity moments indicate that it is within a few percent of hydrostatic equilibrium (Iess et al. 2010). An additional check on the degree to which a body is hydrostatic can be obtained if the degree-two shape is known (see Sect. 3.4 below). Indeed, if both the shape and the gravity are known, the non-hydrostatic components can be subtracted out and the MoI determined from the remaining hydrostatic values (e.g., Hemingway et al. 2018).

Unfortunately, although C_{22} is known from Galileo data, we currently do not have a good enough measurement of J_2 (= $-C_{20}$) to determine whether Europa is hydrostatic. The reason is that Galileo's flybys were mostly equatorial, so the pole-to-pole variation in acceleration (J_2) is poorly constrained from the six Europa flybys.

Figure 10 shows estimates of J_2 and C_{22} from the Galileo data by three different groups. Two of the solutions simply fix J_2 to be $10C_{22}/3$; the third solves for J_2 independently, but obtains a very large uncertainty. Thus, while the gravity moments are consistent with Europa being hydrostatic, we do not know this to be the case. As a result, derivations of moment

Fig. 10 Modified from Gomez Casajus et al. (2021), showing different estimates of J_2 and C_{22} for Europa, with and without the hydrostatic assumption. Note that J_2 is much more poorly constrained than C_{22}, owing to the flyby geometries. For comparison, the expected measurement uncertainties by Europa Clipper are shown to scale (the ellipse orientation also indicates low correlation)
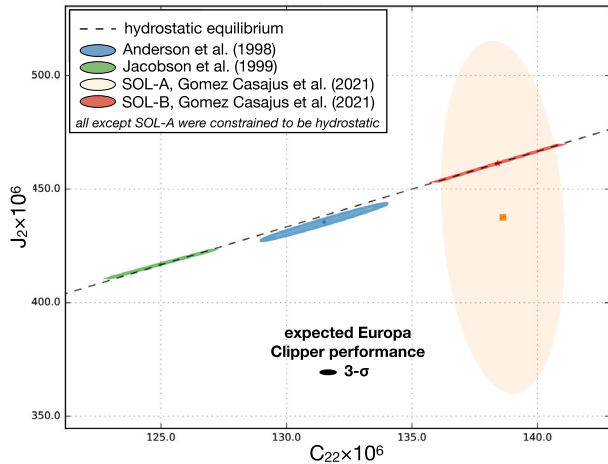
of inertia and hydrosphere thickness (Schubert et al. 2009) must be regarded as provisional. Io and Ganymede's J_2 and C_{22} are consistent with hydrostatic equilibrium (Schubert et al. 2004), and this has been used to argue that Europa should be hydrostatic as well. Each satellite is unique, however, and new data and reanalysis can lead to re-evaluation (e.g., Gomez Casajus et al. 2021), so it is critical that the question of Europa's hydrostatic state be addressed by Europa Clipper.

Because of its multiple flybys, including high-latitude passes, Europa Clipper will determine J_2 and C_{22} independently and to relatively high accuracy. From the uncertainty values shown in Table 5, a 1% departure from hydrostatic behavior should be detectable. If Europa is found to be hydrostatic, the MoI can be inferred directly (Sect. 3.4). If it departs slightly from hydrostatic equilibrium, it may be possible to remove or at least constrain the non-hydrostatic contribution and still determine the MoI, as was previously done at Enceladus by Iess et al. (2014) and McKinnon (2015). Determination of higher order gravity and/or identification of gravity anomalies (i.e., mascons) should constrain the contribution of lateral internal density variations to the degree-2 gravity signal as well. For example, the gravity anomalies measured by Palguta et al. (2006, 2009) for Ganymede would be insufficient to compromise Europa's global hydrostatic state.

3.3.2 Thermal State Constraint

As argued in Sect. 3.1.3.2, at long wavelengths effects from the ocean-rock interface are likely to dominate the gravity signal (Fig. 11). These anomalies might then be used to constrain the thermal state of the silicate interior of Europa.

Pauer et al. (2010) first considered anomalies arising from a synthetic sea floor; however, the pattern of the anomalies will not be particularly diagnostic of activity (Sessa and Dombard 2013), especially with Europa Clipper's very limited spatial sampling and corresponding low resolution global gravity field (cf. Figure 8b). Instead, the magnitude of any gravity anomalies might be more useful. As shown in Pauer et al. (2010), Dombard and Sessa (2019), and Koh et al. (2022), gravity anomalies arising from the sea-floor will be compensated at longer wavelengths by topography on a deeper crust-mantle boundary, under the reasonable assumption that Europa possesses a lower density silicate crust on top of a
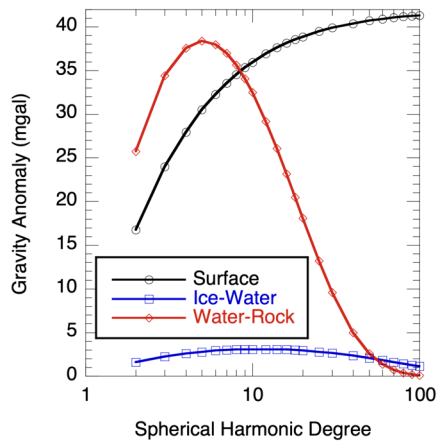
Fig. 11 The maximum surface gravity anomaly for 1-km maximum zonal harmonic topography, uncompensated, on different interfaces in Europa's near-surface. Here, the surface has a density contrast of 1000 kg m^{-3}, the ice-water interface has a density contrast of 100 kg m^{-3} at a depth of 20 km, and the rock-water interface has a contrast of 2000 kg m^{-3} at a depth of 100 km. The rock-water interface dominates the free-air gravity at the longest wavelengths (up to degree ∼10, or roughly 1000 km) and the Bouguer gravity (i.e., subtracting the gravity of the surface topography) at intermediate wavelengths (up to degree ∼50, or roughly 200 km). The results scale with the input topographic amplitude; the higher-order effects of finite amplitude topography (Wieczorek 2007) are negligible. From Dombard and Sessa (2019)
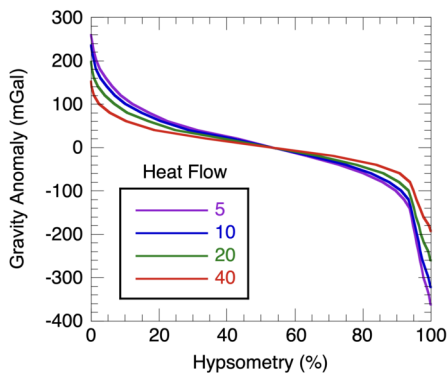
Fig. 12 An example of a gravity "hypsometry" (i.e., the areal percentage of the surface at a particular value of gravity anomaly or higher) from Europa's silicate interior, taken from Dombard and Sessa (2019). Extrema values are larger for heat flows without a strong tidal contribution ($<10 \text{ mW/m}^2$), suggesting that the maximum magnitudes of the gravity anomalies sampled by Europa Clipper could reveal the thermal state of the silicate core, with implications for the habitability of Europa's seafloor. (Heat flow values in mW/m^2)

denser mantle like all other silicate worlds. Thus, dependent on lithospheric strength, Dombard and Sessa (2019) tied this compensation and hence the magnitude of gravity anomalies that Europa Clipper might sense to the heat flow coming out of the silicate core, possibly distinguishing between solely radiogenic heat versus a tidal contribution (Fig. 12). A tidal contribution could be significant for Europa's habitability because a higher heat flow increases the chances of shallower silicate melting that could more easily rise to the sea floor,

providing a mixing zone that could recharge redox gradients and provide nutrients to potential microbial communities.

All of these studies of sea-floor gravity anomalies, however, hinge on the assumption that the topographic characteristics behave like those of the terrestrial worlds: a horizontal scale-dependent power law with similar slopes and amplitudes of order 10 km. The power laws of shape and gravity of various diverse planetary bodies have been empirically observed to follow such laws (e.g., Ermakov et al. 2018). Given the isolation of Europa's sea floor under an ocean with possibly strong currents, this interface could conceivably be a lot flatter. This sea floor, however, may not be as isolated to the production of regional scale topography, as the transient craters for basin-scale impacts on terrestrial worlds can reach hundreds of km deep, enough to have affected Europa's sea floor (though admittedly such would have occurred billions of years ago; Dombard and Sessa 2019; Cunje and Dombard 2022). In addition, it is reasonable to expect Europa's sea floor to have topography that follows these characteristics because of their consistency across a range of environments and geologic processes: currently active Earth and Venus with their thick hydrosphere/atmospheres versus anciently active Mercury and the Moon more dominated by impacts, with Mars somewhere in between. Indeed, the most common factor that might control these topographic characteristics appears to be the rocky material, with a host of geological processes producing power-law topography with amplitudes that create stresses approaching the yield strength of the material. Fortunately, Europa's sea floor shares this material (i.e., silicates). Europa Clipper observations may be able to distinguish among different styles of geologic processes expressed on the Europa seafloor (Koh et al. 2022).

Another way of obtaining information on the thermal state of the silicate shell is the measurement of the k_2 phase lag. The tidal potential Love number of second degree is discussed in Sect. 3.1. As noted, it is a complex number with amplitude and phase. The phase lag between the tidal excitation by Jupiter and the response of the planetary material (silicate rock and/or ice) is a direct measure for Europa's dissipative state. The dissipation rate is proportional to $|k_2|\sin(\delta_2) \approx \mathrm{Im}(k_2)$, with $|k_2|$ the elastic Love number and, δ_2 the phase-lag of the gravity field's second-degree distortion. Depending on the rheological state, in particular viscosity and rigidity of the silicate layer, the dissipation rate in Europa's silicate shell can reach values up to several 10^{11} W (Sotin et al. 2009; Běhounková et al. 2021), at least intermittently (Bland and Elder 2022). Assuming an interior model with a subsurface ocean, the phase lag can reach values of up to a few degrees (e.g., Moore and Schubert 2000) in the case of partial melt in the silicate layer. Detecting this phase lag by gravity measurements would be indicative of a highly dissipative interior. Similarly, measurements of the h_2-k_2 phase lag difference (Sect. 3.1.2) would help identify a warm silicate interior. However, at least for k_2, caution has to be taken, due to possible contributions from the ice shell. If the ice shell is thick and dissipative, it will contribute to the measured phase lag. However, a highly dissipative silicate layer would, in equilibrium, be paired with a thin (non-convecting) ice shell that would preferentially deform elastically (i.e., zero phase lag) in response to the tidal forcing. Obtaining measurements for the thickness and thermal state of the ice shell are thus crucial to interpret a k_2 phase-lag measurement. Whether the latter will be possible depends to a large extent on the actual state of Europa.

3.4 Deep Interior

The G/RS investigation will address the interior structure and the degree of internal differentiation of the icy moon. Two independent methods may be used to retrieve the MoI given some assumptions, from measurements of the degree 2 gravity field coefficients and of the pole obliquity of Europa.

As explained in Sect. 3.3.1, the mean MoI I may best be obtained from J_2 and C_{22} if Europa is verified to be in hydrostatic equilibrium. It can be computed by using the RDA formula for synchronously rotating satellites, deformed by rotation and tides (e.g., Van Hoolst et al. 2008), as follows:

$$\frac{I}{MR^2} = \frac{2}{3}\left(1 - \frac{2}{5}\sqrt{\frac{5}{3\Lambda_{2,0}+1} - 1}\right) \tag{4}$$

where the response coefficient $\Lambda_{2,0} = 2J_2/5q$ (and $q = \omega^2 R^3/GM$, the ratio of centrifugal to gravitational accelerations, where R and ω are the body radius and angular rotation rate), because the tidal potential is three times the rotational potential in peak amplitude (e.g., Hubbard 1984). The current estimates of J_2 and C_{22} by independent analyses of Galileo data result in a range of I/MR^2 from 0.34 to 0.3547 (Fig. 10), which is significantly wider than the formal uncertainty of these gravity solutions ($\sigma_{MoI} \approx 0.0025$). An unconstrained measurement of Europa's degree-2 gravity is thus fundamental to determine whether the moon is in hydrostatic equilibrium, and, consequently, to use the RDA to obtain its mean MoI. Europa Clipper will provide a near-uniform coverage of the icy moon's surface in both latitude and longitude, enabling a robust unconstrained estimation of the degree-2 coefficients. Indeed, we expect the correlation of J_2 and C_{22} in our gravity solution to be low (<0.15). If the estimate of J_2/C_{22} is close to the hydrostatic equilibrium ratio, the RDA will allow us to retrieve the mean MoI with a formal uncertainty of $\sim 1 - 1.5 \times 10^{-4}$.

Departures from hydrostaticity would prevent a direct application of this primary method to measure Europa's MoI. As explained above (Sect. 3.3.1), small non-hydrostatic components due to the ice shell could be corrected, by using the degree-2 shape that will be measured by combining Europa Clipper imaging, altimetric, and stellar occultation data (e.g., Abrahams et al. 2021). An alternative approach to recover the internal mass distribution of Europa is through the determination of the polar moment of inertia, C, by using the degree-2 gravity and the pole obliquity, ϵ. Synchronous bodies are expected to be, to first approximation, locked in the Cassini state (Baland et al. 2012), which provides a formula to compute the C/MR^2 as function of J_2, C_{22}, and ϵ. This equilibrium condition is determined by the coplanarity of the spin axis, the normal to the orbital plane, and the Laplace pole (e.g., Ward 1975). The relative orientation of these unit vectors defines one of the four possible Cassini states. If Europa fulfills this equilibrium condition, the dimensionless polar moment of inertia is given by:

$$\frac{C}{MR^2} = \frac{2}{3}\frac{n}{\dot{\Omega}}\left(\frac{\sin i}{\sim (i+\epsilon)} - 11\right)(J_2 + 2C_{22}) \tag{5}$$

where $i = 0.530518°$ is the orbital inclination with respect to the Laplace plane, $\dot{\Omega} = -11.919505° \; y^{-1}$ is the orbital precession rate, and $n = 101.374724° d^{-1}$ is the orbital mean motion. For a polar moment of inertia consistent with the measured MoI, the obliquity should be in a range of 0.04-0.08°, which we use when evaluating the expected formal uncertainty of $\frac{C}{MR^2}$ that can be obtained by the G/RS investigation.

An unconstrained solution of the pole right ascension and declination in the gravity inversion leads to a large uncertainty of the pole obliquity (Table 5) relative to the expected value. This approach is thus not adequate to retrieve the polar moment of inertia to an uncertainty level able to constrain the interior structure. Applying an a priori constraint to enforce the Cassini state (that is, forcing the pole to be in the plane defined by the normal to the
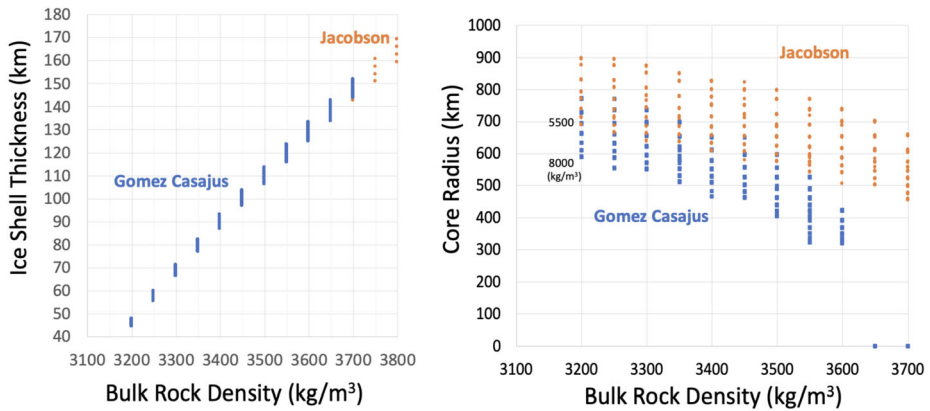
Fig. 13 Inversion of the normalized moment of inertia value by Gomez Casajus et al. (2021) and Jacobson et al. (2000) for a three-layer interior structure (water shell, rocky mantle, and metallic core)

orbital plane and the Laplace pole), the pole estimation may be improved. Alternatively, the pole position and thus the obliquity of the ice shell measured from EIS imagery may be used in Eq. (5). A knowledge of the pole obliquity to 0.05 arcmin would correspond to an uncertainty of the polar moment of inertia of 0.004. The moment of inertia thus derived may then be compared with the moment of inertia derived purely from the gravity moments and the hydrostatic assumption (see above). If the two values are the same, we have a more robust MoI. If they are not the same, then either Europa is not in a Cassini state, or it is not hydrostatic, or (most likely) the shell is decoupled from the interior and has a different obliquity. The latter is the case at Titan (Bills and Nimmo 2011; Baland et al. 2011).

Figure 13 illustrates the interpretation of the normalized moment of inertia values derived by Gomez Casajus et al. (2021) and Jacobson et al. (2000) (under hydrostatic assumption; see Fig. 10) in terms of a three-layer interior model (hydrosphere, silicate mantle, metallic core). This figure shows the greater sensitivity of the moment of inertia to the metallic core radius over the position of the hydrosphere-mantle interface. The difference in core radius illustrated here can be traced back to the bulk metal content (especially iron) and oxidation state of the material from which Europa accreted (e.g., Kuskov and Kronrod 2005).

The projected increase in knowledge of interior structure properties from the Europa Clipper gravity data are illustrated in Fig. 14 for the precision on the moment of inertia expected from the future Europa Clipper gravity observations. The projected increase in constraining the hydrosphere thickness is marginal. Under the assumption of hydrostatic equilibrium, a projected 10× increase in precision over the Gomez Casajus et al. (2021) results would somewhat decrease the space of possible metallic core radius and bulk rock density.

Low-degree terms in the gravity field, beyond degree-2, also provide information on the deep interior. Even zonal harmonics (such as $J_4 = -C_{40}$) are sensitive to higher moments of the radial density distribution, and so can provide additional constraints on layering within Europa. Other harmonics are sensitive to Europa's non-hydrostatic density distribution, such as caused by density, temperature, and as per Fig. 11, topographic anomalies. While it may be difficult to untangle hydrostatic and non-hydrostatic contributions in practice, it should be possible to at least put constraints on the nature of these contributions. Forward modeling of, for example, thermal anomalies due to solid state convection and/or melting in Europa's
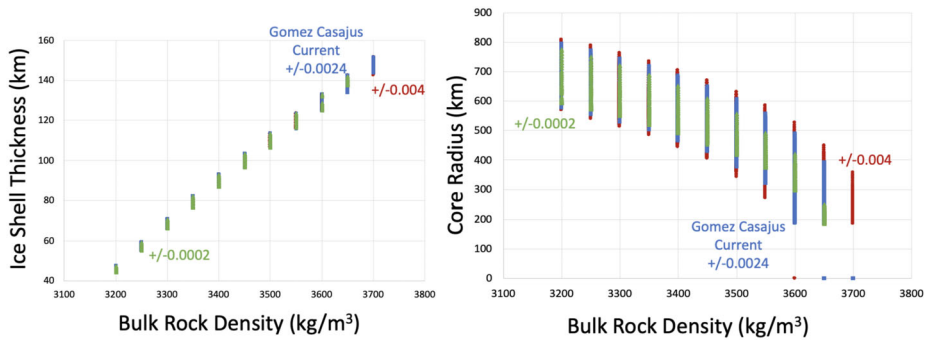
Fig. 14 Same as Fig. 13 but for projected precision of $\sim 2 \times 10^{-4}$ (green), under hydrostatic assumption applies to the Gomez Casajus model

silicate mantle (Běhounková et al. 2020) would be valuable in setting such constraints, once Europa Clipper gravity data is obtained.

3.5 Jupiter System Evolution

The Laplace resonance excites the eccentricity of Europa's orbit around Jupiter, which in turn is responsible for significant tidal heating. However, the tidal dissipation inside the satellite tends to reduce its eccentricity, introducing a complex coupling between the internal structure and the orbital evolution, still far from being fully understood (Ojakangas and Stevenson 1986; Hussmann and Spohn 2004). Moreover, the tides raised by each of the three moons (Io, Europa, and Ganymede) on Jupiter in turn modify a given moon's semimajor axis, and this in turn affects the orbits of the other two, due to their resonant interaction, further complicating the dynamics (see Steinbrügge et al. 2023). Recent measurements suggest that the tidal dissipation of Saturn is higher than predicted by standard tidal theories, and that it is not constant between the different satellites, in agreement with the resonance locking tidal theory (Lainey et al. 2012; Fuller et al. 2016; Lainey et al. 2017, 2020). Characterizing the tidal dissipation of Jupiter helps constrain the past evolution of Europa's orbit, with consequences on assessing its habitability: if the Galilean moons were locked into the Laplace resonance early in the history of the Jupiter system, then the subsurface liquid ocean may have existed for a geologically extended period of time, one possibly sufficient for prebiotic chemistry to evolve to the production of complex organic molecules and life to start and develop (Hand et al. 2009; Vance et al., this collection).

The Europa Clipper Doppler data acquired during all close encounters will provide critical information on Europa's ephemerides. Doppler data acquired near the closest approach are very sensitive to the relative position of the spacecraft with respect to the moon. Outside the sphere of influence of Europa, which has a radius of about 10000 km, the data are sensitive to the relative position of the spacecraft with respect to Jupiter. During a close encounter, Europa Clipper remains within the sphere of influence of the moon for only about 30 minutes. The expected performance in the estimation of Europa ephemeris was assessed with simulations. The formal uncertainty in Europa's measured position is 5-10 m in the radial direction, 10-100 m along track, and $\sim$1 km normal to the orbital plane (Fig. 15). One of the key factors affecting Europa's orbital motion is the Laplace resonance with Io and Ganymede. Therefore, a combination with the radiometric and astrometric data from other space missions, such as Galileo, Juno, and JUICE, will improve the estimation of Europa's orbit and Jupiter's dissipation (Magnanini et al. 2022).

Fig. 15 Expected accuracy of Europa's orbit (position uncertainty with respect to the Jupiter Barycenter) in the radial, along-track, and normal directions

Europa wrt Jupiter Barycenter
Position Uncertainty (RTN)
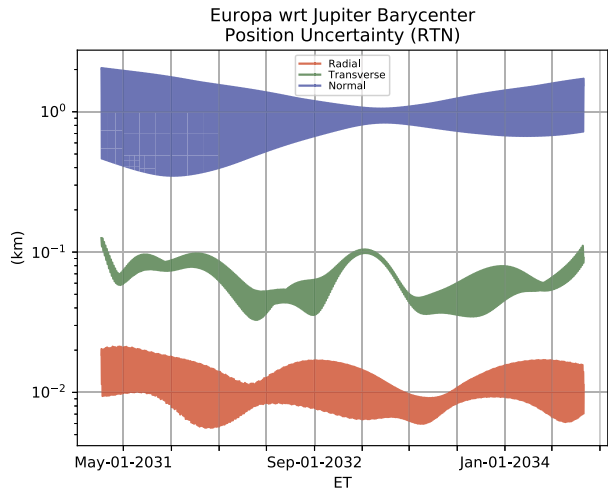
4 Radio Science Measurements

4.1 Europa Ionosphere Observations

At the conclusion of the Europa Clipper mission, the G/RS investigation will have comprehensively mapped the spatial structure of the ionosphere, determining how plasma densities vary with altitude, geographic location, and geometry with respect to magnetospheric interactions. In conjunction with complementary observations by other Europa Clipper investigations, these G/RS measurements will address fundamental questions about the nature of Europa's ionosphere and its relationships with Europa's surface, Europa's neutral atmosphere, and Jovian magnetosphere. Furthermore, by characterizing the impact of Europa's ionospheric plasma on radio science measurements of Europa's gravity field and on magnetometry measurements of Europa's induced magnetic field, these ionospheric observations will also enhance Europa Clipper's ability to determine the geophysical properties of Europa's interior.

The frequency residual Δf, observed frequency minus predicted frequency, satisfies (Eq. (3) of Phipps and Withers 2017):

$$\Delta f = \frac{2e^2}{8\pi^2 m_e \varepsilon_0 c f} \left(\frac{dQ}{dt} \right) \tag{6}$$

where $Q = \int N \, dl$ is the total electron content along the ray path, c is the speed of light, t is time, l is distance along the ray path, e is the electron charge, m_e is the electron mass, ε_0 is the permittivity of free space, and N is the electron density. The factor of 2 in the numerator accounts for the two-way path. Equation (6) is integrated with respect to time to find $Q(t)$. Possible systematic errors (e.g., trajectory uncertainties caused by imperfect knowledge of Europa's gravitational field) are removed with a standard high-altitude baseline correction such that $Q = 0$ when the ray path is far above the ionosphere (e.g., Phipps et al. 2018; Dalba and Withers 2019). The ionosphere is divided into spherical shells of uniform electron density (Fig. 16). Using the spacecraft trajectory, the path lengths dl through each shell are found for each ray path such that a given total electron content value Q_i equals $S \, N_j \, dl_{ij}$ where i labels a ray path and j labels a spherical shell. Inversion of this matrix relationship
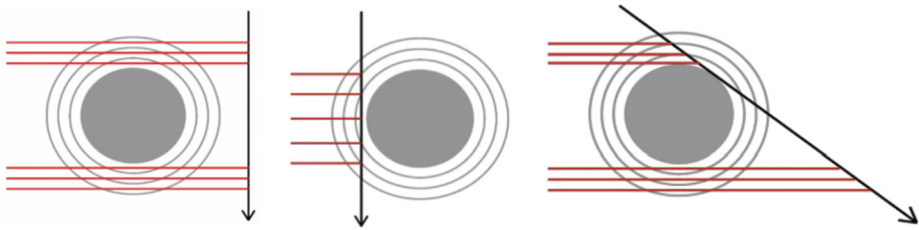
Fig. 16 Three classes of occultation. Europa is shaded grey, spacecraft trajectory is the black arrow, ray paths to Earth are red lines, and grey circles are spherical shells of uniform electron density. Successive red lines sample different sets of spherical shells. (left) Traditional occultation. (middle) "Virtual" occultation. (right) "Real" occultation with "in situ" on ingress (upper set of red lines) and "remote" on egress (lower set of red lines)

yields the electron density N as a function of radial distance r and hence altitude, z. We have already developed and successfully demonstrated this matrix-based method on Cassini occultations at Saturn (Tamburo et al. 2019). Mitigation plans for possible limitations of the assumption of spherical symmetry (McGrath et al. 2004) will be assessed in development.

In a traditional radio occultation (left panel of Fig. 16), the spacecraft is above the ionosphere during the observing period. Europa Clipper offers other occultation scenarios (middle and right panels of Fig. 16). In a "remote, real" (or traditional) occultation, the spacecraft is occulted and the spacecraft is above the ionosphere throughout the observing period. In an "in situ, real" occultation, the spacecraft is occulted, but the spacecraft is within the ionosphere during the observing period. In a "virtual" occultation, the spacecraft is not occulted and the spacecraft is within the ionosphere during the observing period. In a "virtual" occultation, ingress and egress electron density profiles are both assigned to the closest approach point. For each "virtual" occultation, we will average ingress and egress profiles and report one profile. Flybys at solar phase angles $\leq 90°$ tend to offer "virtual" occultations. Flybys at solar phase angles $\geq 90°$ tend to offer "real" occultations in which one part is "remote" (traditional) and the other is "in situ".

The spatial coverage of radio occultation observations is highly complementary to the coverage of in situ plasma measurements. In situ plasma measurements are concentrated on the magnetospheric flanks, whereas radio occultations can provide data within 60° of either the magnetospheric ram or anti-ram points (Fig. 17). They also provide the closest observations to Pwyll Crater, site of persistent plume activity (Sparks et al. 2017).

4.2 Io Plasma Torus

As highlighted in Sect. 2.1.2, the Io Plasma Torus (IPT) will induce a non-negligible non dynamical Doppler shift on the Europa Clipper radio links, when the spacecraft is occulted by the IPT as seen from Earth. This Doppler shift is proportional to the rate of change of the TEC, the integrated electron density along the line-of-sight direction. However, from the point of view of gravity science at Europa, this effect is an undesirable source of systematic error. It will be mitigated by subtraction of a prediction for the Doppler shift caused by the IPT. Initially, such predictions will be based on IPT models, which were derived mainly by using Doppler data acquired by the Juno mission to Jupiter (Phipps and Withers 2017; Phipps et al. 2018; Phipps et al. 2019; Zannoni et al. 2020; Phipps et al. 2020; Phipps et al. 2020). However, it is hoped that Europa Clipper will conduct similar radio occultation observations of the IPT. Such observations during the Europa Clipper epoch would improve
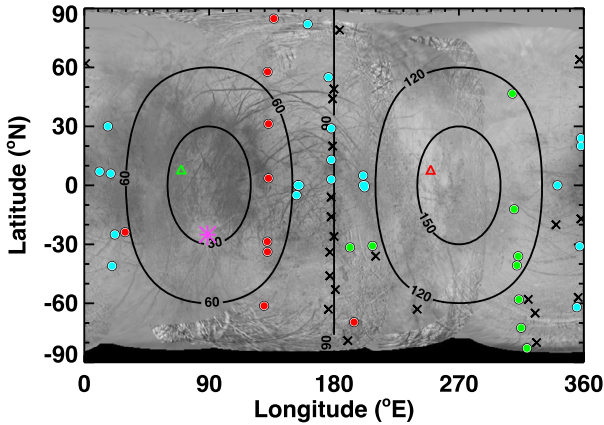
Fig. 17 Projected geographic coverage for the trajectory 19F23. Contours are angular distance from the magnetospheric ram point of 0° N, 90° E. "Real" ingress occultations are red disks, "real" egress occultations are green disks, "virtual" occultations, which are also flybys<100 km, are cyan disks, and other flybys<100 km are black Xs. The non-flyby "real" ingress and egress occultations are marked by triangles. The magenta asterisk marks Pwyll Crater at 25° S, 89° E, the location of significant plume activity. The background image is the Voyager - Galileo SSI Global Mosaic from US Geological Survey (2002)

Fig. 18 Expected IPT-induced range-rate at 60 second integration time for the 51 flybys, for the trajectory tour 19F23
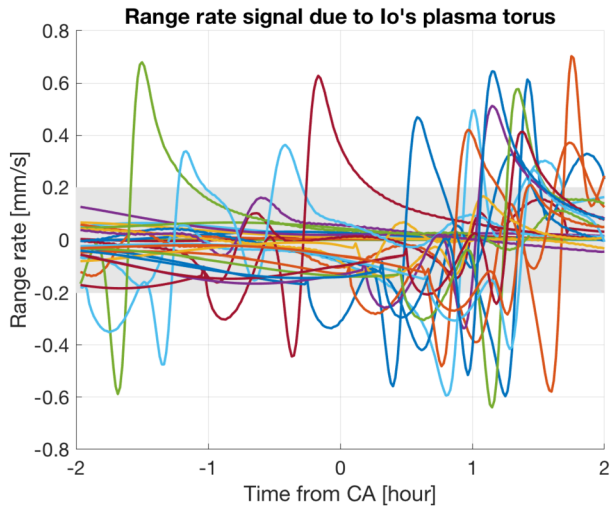
constraints on temporal and longitudinal variabilities of the IPT electron density (Moirano et al. 2021). The expected range-rate due to the IPT for the tour trajectory 19F23 is shown in Fig. 18.

From the range rate peaks depicted in Fig. 18 it is clear that the expected noise level in the Doppler observables (introduced in Sect. 2.1.3.2) will be low enough to allow observability of the IPT-induced Doppler signatures, even in the noisier conditions (0.2 mm/s at 60 s integration time for $10° <$ SEP angles $< 20°$). The geometry of the IPT radio occultations by Europa Clipper is shown in Fig. 19.
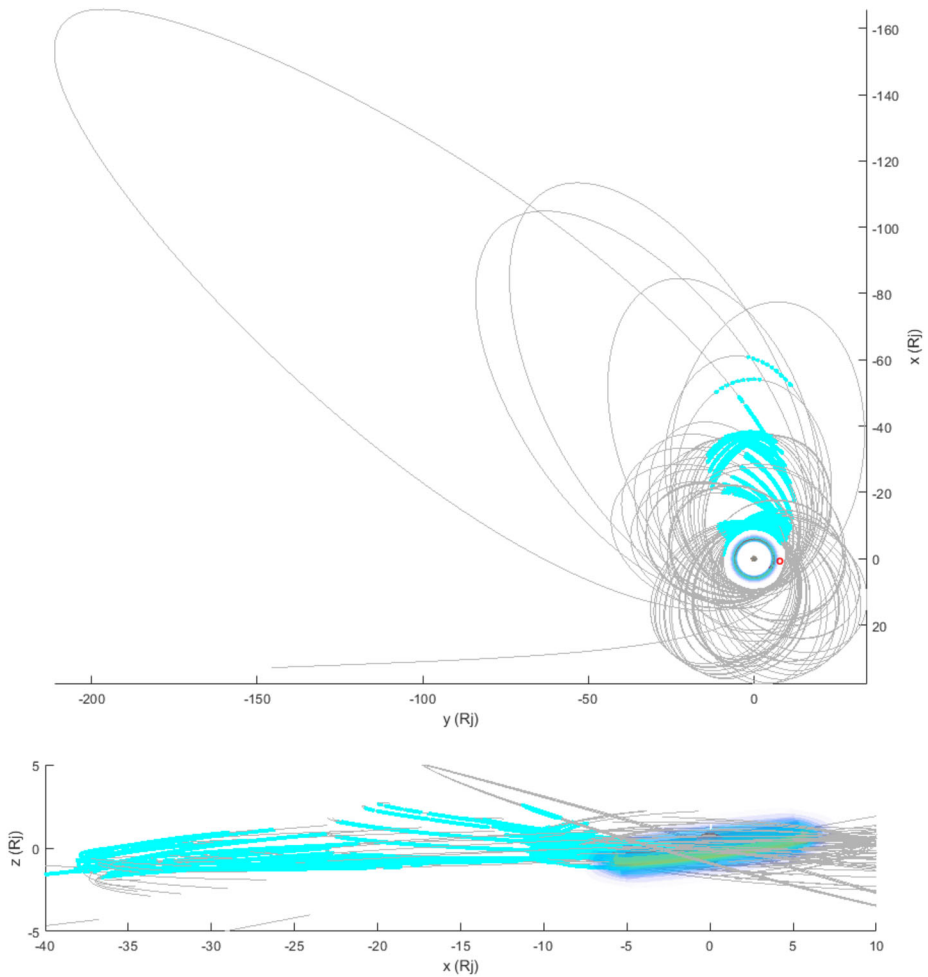
Fig. 19 Geometry of the IPT radio occultations by Europa Clipper for tour 19F23, in a Jupiter-Sun-Orbit Frame (JSO; +X in Sun-Jupiter direction and +Y in Jupiter velocity direction)

While the IPT occultations by the Juno spacecraft were mostly relatively fast and polar in the Prime Mission, in the Extended Mission they changed their orientation, getting closer to Jupiter's equatorial plane, to cross the IPT along paths almost aligned with Jupiter's centrifugal equator, similarly to the geometries expected for Europa Clipper. The temporal separation between the end of the Juno mission and the Europa Clipper tour (about 7 years) will allow to fine-tune long-term evolution models of the IPT and their correlation with Io's volcanic activity.

5 Data Products and Archiving

The Gravity/Radio Science investigation relies on measurements of the Doppler shift of the radio link between the Deep Space Network and the Europa Clipper Spacecraft. The Doppler

shift measurements are taken as a function of time during closest approach encounters with Europa. Operationally, this measurement is made by comparing the radio frequency which was transmitted with the radio frequency which was received. The investigation utilizes the highly-stable frequency reference of the DSN to transmit the uplink radio signal to the spacecraft. The spacecraft transponder then phase-coherently retransmits the signal back to the DSN (essentially acting as a "mirror"), which is then recorded by the sensitive receivers in the DSN. Fundamentally, this means that the primary measurement – the Doppler frequency observable – is generated entirely by the DSN, and not the spacecraft.

Two primary raw data types are produced by the DSN and used by the G/RS team for the purposes of the investigation. The first is called closed-loop radiometric tracking data, which is generated by the DSN's Block V Closed-Loop receiver. The closed-loop radiometric tracking data contains precise measurements of the frequency. Due to the low link margin using the LGA and FBA antennas, the closed-loop receiver will not be able to maintain a reliable lock on the signal received from the spacecraft in the phase-locked tracking loop of the receiver. However, the signal can be captured by the DSN Open Loop Receiver (OLR) which does not require a tracking loop to record the signal. The OLR measures the down-converted antenna voltage in In-Phase and Quadrature samples. The DSN maintains and produces a standard set of data products for each of these types.

The raw data collected by the DSN receivers must be calibrated for propagation effects. As the radio signal propagates from the DSN to the spacecraft and back, it encounters several effects that must be considered. The signal will pass through Earth's troposphere and ionosphere, both of which impart a small phase delay on the radio signal. The DSN's Tracking System and Analytic Calibration (TSAC) subsystem provides daily calibrations for these effects using measurements from local meteorology stations and Global Positioning Satellites. Three data products provide Earth propagation calibrations: the troposphere calibration product, the ionosphere calibration product, and the DSN weather product. Like the tracking data products, the DSN maintains and produces these as a standard set of data products.

G/RS data can be extracted and calibrated from these data products. Calibrated data products will be produced by extracting Doppler frequency observables from the OLR data using frequency estimation techniques (e.g., phase-locked loop, fast Fourier transform). The extracted Doppler frequency observables will be calibrated for known propagation effects. Calibrated data are provided in the CCSDS Tracking Data Message standard format. The precise uplink frequency from the closed-loop data is also recorded in the calibrated data files.

Ancillary data are required to properly interpret the calibrated Doppler frequency observable measurements. To compute a predicted frequency, the position and timing of Earth's orientation in space and the position of the spacecraft antenna phase centers must be known relative to the spacecraft center of mass. The Earth Orientation Parameters (EOP) data product is produced daily by JPL and provides knowledge of the Earth's precise rotational state and UTC timing offsets. Although the offset of the phase center of each antenna is known from mechanical assembly drawings of the spacecraft, G/RS will utilize several of these antennas during a given encounter and thus the time history of antenna use must be known. This information is derived from spacecraft commanding and telemetry streams. With knowledge of which antenna is active at a given time and spacecraft attitude information (archived with the Navigation and Ancillary Information Facility of the PDS), the antenna phase center can be precisely computed.

For gravity science investigations, the spacecraft's trajectory must also be modeled. Of particular interest are non-gravitational forces, such as solar radiation pressure, albedo pressure, and spacecraft thruster firings. Spacecraft thruster firings are documented in a Small

Table 6 Gravity/Radio Science data bundles delivered to the PDS Geosciences Node

PDS4 Data Level	Delivery Frequency	Included Data Types
Raw	Every 6 months	Open-Loop Tracking Data
		Closed-Loop Tracking Data
		DSN Troposphere Media Calibration
		DSN Ionosphere Media Calibration
		DSN Surface Meteorology Files
		Earth Orientation Parameters
		Spacecraft Small Forces Files
		Spacecraft Antenna Time History
		Spacecraft Mass History
Partially Processed / Calibrated	Every 6 months	Processed Open-Loop Doppler Data
		Processed Transmit Frequency Profile (Ramps)
Derived	6 months after EOM	Line-of-Sight (LOS) Doppler Residuals
		Europa Ionosphere Electron Density Profiles
		Europa Gravity Field Spherical Harmonic Coefficients
		Europa Gravity Field Covariance
		Europa Gravity Field Maps

Forces File, which provides a history of thruster firings, directions, and velocities. Furthermore, modeling non-gravitational forces requires knowledge of the spacecraft's mass at a given time. This information is assembled and documented in a Spacecraft Mass History file.

All Europa Clipper Gravity/Radio Science data products will be archived with the Geosciences Node of NASA's Planetary Data System (PDS). Data products will be grouped into bundles by data processing level: Raw (NASA Level 0), Calibrated (NASA Level 1A), and Derived (NASA Level 2) as shown in Table 6. Each data product and bundle will be compliant with the PDS4 standard and include all necessary documentation. The Raw data product bundle will include closed-loop and open-loop radiometric tracking from the Deep Space Network alongside the media calibration data and ancillary data. Raw data products will be in their original form as generated by the DSN. The Calibrated data product bundle will include Doppler observables extracted from the open-loop tracking data and the DSN uplink frequency profile extracted from the closed-loop tracking data. During the Europa Clipper prime mission, Raw and Calibrated data bundles will be updated every 6 months on the PDS.

Derived data are generated using data products from the Raw and Calibrated bundles with the methods described in Sect. 2. The orbit determination process ingests the Doppler frequency observables and produces an estimate of the gravitational field, associated uncertainties, and residual frequency. These are provided as a line-of-sight (LOS) Doppler residuals product, gravitational field coefficients and uncertainties, and gravitational field maps. Analysis of the frequency residuals during radio occultation geometries yields vertical electron density profiles of Europa's ionosphere, also included as a derived data product. Derived data products will be nominally delivered 6 months after end of mission (EOM), but may be provided on an earlier schedule to facilitate data analysis.

6 Conclusion

The Gravity/Radio Science investigation of Europa Clipper will measure the tidal response of Europa to Jupiter's forcing, complementing the diverse investigations by the Europa Clipper payload of Europa's ice shell, ocean, and interior. The radio tracking data collected during the dozens of well-distributed flybys will also allow Europa Clipper to ascertain whether Europa is in hydrostatic equilibrium, to constrain the internal structure of Europa from down to its putative metallic core, to measure its low-degree gravity field to uniquely probe the rocky interior's thermal and physical state, and to refine the Laplace resonance and address the long-term evolution of the Jovian satellites. In combination with data from other instruments, new or better constraints on the ice shell and the subsurface ocean will be possible. Complementary compositional constraints from ECM, h_2 estimates from REASON, and compositional data from other instruments are required in order to increase the accuracy of the shell thickness derived from inversion of k_2. Radio occultations will also return profiles of its ionosphere to better understand Europa within the complex Jupiter system. The G/RS investigation will be an intrinsic part of the Europa Clipper exploration of Europa, addressing some objectives uniquely and affording distinct sensitivity to benefit the comprehensive knowledge of Europa necessary to truly understand its potential habitability.

Glossary

APL	Applied Physics Laboratory
CoM	center of mass
DTT	Downlink Tracking and Telemetry
DSN	Deep Space Network
DTM	Digital Terrain Model
FBA	Fanbeam Antennas
FFT	Fast Fourier Transform
FTS	Frequency and Timing System
GN&C	Guidance, Navigation and Control
G/RS	Gravity and Radio Science
HEMT	High Electron Mobility Transistor
HGA	High Gain Antenna
IF	Intermediate Frequency
IQ	In-phase and Quadrature
IPT	Io Plasma Torus
LCP	Left-Circularly Polarized
LGA	Low Gain Antenna
LOS	Line-of-sight
MGA	Medium Gain Antenna
MoI	moment of inertia
MONTE	Mission Analysis, Operations, and Navigation Toolkit Environment
OD	Orbit Determination
OLR	Open-Loop Receiver
PDS	Planetary Data System
RCP	Right-Circularly Polarized
REASON	Radar for Europa Assessment and Sounding: Ocean to Near-surface
RRT	Receiver, Ranging, and Telemetry
SEP	Sun-Earth-Probe angle
SNR	Signal-to-Noise Ratio

TEC   Total electron content
TWTA   Traveling Wave Tube Amplifiers
USO   Ultra Stable Oscillator

Declarations

Competing Interests The authors declare that they have no conflict of interest.

References

Abrahams JN, Nimmo F, Becker TM, Gladstone GR, Retherford KD, Steinbrügge G, Mazarico E (2021) Improved determination of Europa's long-wavelength topography using stellar occultations. Earth Space Sci 8(7):e2020EA001586. https://doi.org/10.1029/2020EA001586

Akiba R, Ermakov AI, Militze B (2022) Probing the icy shell structure of ocean worlds with gravity-topography admittance. Planet Sci J 3:53. https://doi.org/10.3847/PSJ/ac4d2b

Anderson JD et al (1992) Gravitation and celestial mechanics investigations with Galileo. Space Sci Rev 60(1):591–610. https://doi.org/10.1007/BF00216869

Anderson JD, Schubert G, Jacobson RA, Lau EL, Moore WB, Sjogren WL (1998) Europa's differentiated internal structure: inferences from four Galileo encounters. Science 281(5385):2019–2022. https://doi.org/10.1126/science.281.5385.2019

Anderson JD, Schubert G, Jacobson RA, Lau EL, Moore WB, Palguta JL (2004) Discovery of mass anomalies on Ganymede. Science 305:989–991. https://doi.org/10.1126/science.1099050

Asmar SW et al (2005) Spacecraft Doppler tracking: noise budget and accuracy achievable in precision radio science observations. Radio Sci 40:2. https://doi.org/10.1029/2004RS003101

Asmar SW et al (2017) The Juno gravity science instrument. Space Sci Rev 213(1):205–218. https://doi.org/10.1007/s11214-017-0428-7

Baland RM, Van Hoolst T, Yseboodt M, Karatekin Ö (2011) Titan's obliquity as evidence of a subsurface ocean? Astron Astrophys 530:A141. https://doi.org/10.1051/0004-6361/201116578

Baland RM, Yseboodt M, Van Hoolst T (2012) Obliquity of the Galilean satellites: the influence of a global internal liquid layer. Icarus 220(2):435–448. https://doi.org/10.1016/j.icarus.2012.05.020

Běhounková M, Tobie G, Choblet G, Kervazo M, Daswani MM, Dumoulin C, Vance SD (2020) Tidally induced magmatic pulses on the oceanic floor of Jupiter's moon Europa. Geophys Res Lett 48:e2020GL090077. https://doi.org/10.1029/2020GL090077

Běhounková M, Tobie G, Choblet G, Kervazo M, Melwani Daswani M, Dumoulin C, Vance SD (2021) Tidally induced magmatic pulses on the oceanic floor of Jupiter's moon Europa. Geophys Res Lett 48(3):e2020GL090077. https://doi.org/10.1029/2020GL090077

Bertone S, Mazarico E, Barker MK, Goossens S, Sabaka TJ, Neumann GA, Smith DE (2021) Deriving Mercury geodetic parameters with altimetric crossovers from the Mercury Laser Altimeter (MLA). J Geophys Res, Planets 126(4):e2020JE006683.

Bills BG, Nimmo F (2011) Rotational dynamics and internal structure of Titan. Icarus 214(1):351–355. https://doi.org/10.1016/j.icarus.2011.04.028

Bills BG, Scott BR (2022) Rotation models for the Galilean satellites. Planet Space Sci 219:105474. https://doi.org/10.1016/j.pss.2022.105474

Bills BG, Nimmo F, Karatekin O, Van Hoolst T, Rambaux N, Levrard B, Laskar J (2009) Pappalardo RT, McKinnon WB, Khurana KK (eds) Rotational dynamics of Europa, in Europa University of Arizona Press, Tucson, pp 119–136

Bland MT, Elder CM (2022) Silicate volcanism on Europa's seafloor and implications for habitability. Geophys Res Lett 49:e2021GL096939. https://doi.org/10.1029/2021GL096939

Boehm J, Schuh H (2004) Vienna mapping functions in VLBI analyses. Geophys Res Lett 31(1):L0160. https://doi.org/10.1029/2003GL018984

Buccino DR et al (2018) Extraction of Doppler observables from open-loop recordings for the Juno radio science investigation. In: 2018 United States national committee of URSI national radio science meeting (USNC-URSI NRSM)

Buccino DR et al (2020) Detecting Juno's 'heartbeat': communications support during critical events of the Juno mission. In: 2020 IEEE aerospace conference. https://doi.org/10.1109/AERO47225.2020.9172616

Buffington et al (2019) G/RS Europa Clipper Capabilities for Gravity/Radio Science. JPL D-103905, available on NSPIRES alongside ROSES C.24 as Clipper+GRS+Capabilities.pdf. https://nspires.nasaprs.com/

Cassidy T et al (2007) The spatial morphology of Europa's near-surface O_2 atmosphere. Icarus 191:755–764. https://doi.org/10.1016/j.icarus.2007.04.033

Castillo J, Mocquet A, Sotin C (2000) Detecting a deep ocean within Europa by means of geodetic measurements. C R Acad Sci 330:659–666. https://doi.org/10.1016/S1251-8050(00)00195-6

Castillo-Rogez JC, Melwani Daswani M, Glein C, Vance S, Cochrane C (2022) Role of non-water ice in driving ocean salinity and electrical conductivity in ocean worlds. Geophys Res Lett 49(16):e2021GL097256. https://doi.org/10.1029/2021GL097256

Cunje AB, Dombard AJ (2022) Investigation impact basin formation on Europa's seafloor. In: Lunar and planetary science conference, vol 1222

Dalba PA, Withers P (2019) Cassini radio occultation observations of Titan's ionosphere: the complete set of electron density profiles. J Geophys Res 124:643–660. https://doi.org/10.1029/2018JA025693

Davies ME, Katayama FY (1981) Coordinates of features on the Galilean satellites. J Geophys Res Space Phys 86(A10):8635–8657. https://doi.org/10.1029/JA086iA10p08635

Dombard AJ, Sessa AM (2019) Gravity measurements are key in addressing the habitability of a subsurface ocean in Jupiter's moon Europa. Icarus 325:31–38. https://doi.org/10.1016/j.icarus.2019.02.025

Durante D et al (2019) Titan's gravity field and interior structure after Cassini. Icarus 2019(326):123–132. https://doi.org/10.1016/j.icarus.2019.03.003

Durante D, Parisi M, Serra D, Zannoni M, Notaro V, Racioppa P, Buccino DR et al (2020) Jupiter's gravity field halfway through the Juno mission. Geophys Res Lett 47:no. 4, e2019GL086572. https://doi.org/10.1029/2019GL086572

Ermakov AI, Park RS, Bills BG (2018) Power laws of topography and gravity spectra of the solar system bodies. J Geophys Res, Planets 123(8):2038–2064. https://doi.org/10.1029/2018JE005562

Ermakov AI, Park RS, Roa J, Castillo-Rogez JC, Keane JT, Nimmo F, Kite ES, Sotin C, Lazio TJ, Steinbrügge G, Howell SM (2021) A recipe for the geophysical exploration of Enceladus. Planet Sci J 2(4):157. https://doi.org/10.3847/PSJ/ac06d2

Evans S, Taber W, Drain T, Smith J, Wu H-C, Guevara M, Sunseri R, Evans J (2018) MONTE: the next generation of mission design and navigation software. CEAS Space J 10:79–86. https://doi.org/10.1007/s12567-017-0171-7

Fjeldbo G, Kliore AJ, Eshleman VR (1971) The neutral atmosphere of Venus as studied with the Mariner V radio occultation experiments. Astron J 76:123–140

Folkner WM et al (2017) Jupiter gravity field estimated from the first two Juno orbits. Geophys Res Lett 44:4694–4700. https://doi.org/10.1002/2017GL073140

Folkner WM et al (2018) The rotation and interior structure experiment on the InSight mission to Mars. Space Sci Rev 214(5):1–16. https://doi.org/10.1007/s11214-018-0530-5.

Fuller J, Luan J, Quataert E (2016) Resonance locking as the source of rapid tidal migration in the Jupiter and Saturn moon systems. Mon Not R Astron Soc 458(4):3867–3879. https://doi.org/10.1093/mnras/stw609

Gao P, Stevenson DJ (2013) Nonhydrostatic effects and the determination of icy satellites' moment of inertia. Icarus 226:1185–1191. https://doi.org/10.1016/j.icarus.2013.07.034

Geeraert JL, Leonard JM, Kenneally PW, Antreasian PG, Moreau MC, Lauretta DS (2019) OSIRIS-REx navigation small force models. In: AAS/AIAA astrodynamics specialist conference, Portland, Maine, USA. AAS paper, pp 19–717

Genova A, Goossens S, Lemoine FG, Mazarico E, Neumann GA, Smith DE, Zuber MT (2016) Seasonal and static gravity field of Mars from MGS, Mars Odyssey and MRO radio science. Icarus 272:228–245. https://doi.org/10.1016/j.icarus.2016.02.050

Genova A, Goossens S, Mazarico E, Lemoine FG, Neumann GA, Kuang W et al (2019) Geodetic evidence that Mercury has a solid inner core. Geophys Res Lett 46(7):3625–3633. https://doi.org/10.1029/2018GL081135

Gomez Casajus L, Zannoni M, Modenini D, Tortora P, Nimmo F, Van Hoolst T, Buccino D, Oudrhiri K (2021) Updated Europa gravity field and interior structure from a reanalysis of Galileo tracking data. Icarus 358:114187. https://doi.org/10.1016/j.icarus.2020.114187

Goossens S, Sabaka TJ, Genova A, Mazarico E, Nicholas JB, Neumann GA (2017) Evidence for a low bulk crustal density for Mars from gravity and topography. Geophys Res Lett 44(15):7686–7694. https://doi.org/10.1002/2017GL074172

Goossens SJ, Rowlands DD, Mazarico E, Liounis AJ, Small JL, Highsmith DE, Swenson JC, Lyzhoft JR, Ashman BW, Getzandanner KM, Leonard JM, Geeraert JL, Adam DC, Antreasian PG, Barnouin OS, Daly MG, Seabrook JA, Lauretta DS (2021) Mass and shape determination of (101955) Bennu using differenced data from multiple OSIRIS-REx mission phases. Planet Sci J 2:6. https://doi.org/10.3847/PSJ/ac26c4

Hand KP, Chyba CF (2007) Empirical constraints on the salinity of the Europan ocean and implications for a thin ice shell. Icarus 189:424–438. https://doi.org/10.1016/j.icarus.2007.02.002

Hand KP, Chyba CF, Carlson RW, Cooper JF (2006) Clathrate hydrates of oxidants in the ice shell of Europa. Astrobiology 6(3):463–482. https://doi.org/10.1089/ast.2006.6.463

Hand KP, Chyba CF, Priscu JC, Carlson RW, Nealson KH (2009) Astrobiology and the potential for life on Europa. In: Pappalardo RP, McKinnon WB, Khurana KK (eds) Europa, pp 589–629

Heiskanen W, Moritz H (1967) Physical geodesy. Freeman, San Francisco

Hemingway D, Iess L, Tajeddine R, Tobie G (2018) The interior of Enceladus. In: Schenk PM et al (eds) Enceladus and the icy moons of Saturn, pp 57–77. University of Arizona Press Tucson. https://doi.org/10.2458/azu_uapress_9780816537075-ch004.

Hinson DP, Linscott IR, Young LA, Tyler GL, Stern SA, Beyer RA, Bird MK, Ennico K, Gladstone GR, Olkin CB, Pätzold M (2017) Radio occultation measurements of Pluto's neutral atmosphere with New Horizons. Icarus 290:96–111. https://doi.org/10.1016/j.icarus.2017.02.031

Howard HT, Eshleman VR, Hinson DP, Kliore AJ, Lindal GF, Woo R, Bird MK, Volland H, Edenhofer P, Pätzold M, Porsche H (1992) Galileo radio science investigations. In: The Galileo mission, pp 565–590. https://doi.org/10.1007/978-94-011-2512-3_21

Howell S (2021) The likely thickness of Europa's icy shell. Planet Sci J 2:129. https://doi.org/10.3847/PSJ/abfe10

Hubbard WB (1984) Planetary interiors. Van Nostrand, New York

Hurford TA, Bills BG, Helfenstein P, Greenberg R, Hoppa GV, Hamilton DP (2009) Geological implications of a physical libration on Enceladus. Icarus 203(2):541–552. https://doi.org/10.1016/j.icarus.2009.04.025

Hussmann H, Spohn T (2004) Thermal-orbital evolution of Io and Europa. Icarus 171(2):391–410. https://doi.org/10.1016/j.icarus.2004.05.020

Hussmann H, Shoji D, Steinbrügge G, Stark A, Sohl F (2016) Constraints on dissipation in the deep interiors of Ganymede and Europa from tidal phase-lag. Celest Mech Dyn Astron 126(1):131–144. https://doi.org/10.1007/s10569-016-9721-0

Hussmann H, Oberst J, Stark A, Steinbrügge G (2018) The BepiColombo Laser Altimeter (BELA): an instrument for geodetic investigations of Mercury. In: Planetary remote sensing and mapping, pp 49–61. https://doi.org/10.1201/9780429505997

Iess L, Rappaport NJ, Jacobson RA, Racioppa P, Stevenson DJ, Tortora P, Armstrong JW, Asmar SW (2010) Gravity field, shape, and moment of inertia of Titan. Science 327(5971):1367–1369. https://doi.org/10.1126/science.1182583

Iess L, Jacobson RA, Ducci M, Stevenson DJ, Lunine JI, Armstrong JW, Asmar SW, Racioppa P, Rappaport NJ, Tortora PIess L et al (2012) The tides of Titan. Science 337:457–459. https://doi.org/10.1126/science.1219631

Iess L, Stevenson DJ, Parisi M, Hemingway D, Jacobson RA, Lunine JI, Nimmo F, Armstrong JW, Asmar SW, Ducci M, Tortora P (2014) The gravity field and interior structure of Enceladus. Science 344(6179):78–80. https://doi.org/10.1126/science.1250551

Iess L, Folkner WM, Durante D, Parisi M, Kaspi Y, Galanti E, Guillot T, Hubbard WB, Stevenson DJ, Anderson JD, Buccino DR (2018) Measurement of Jupiter's asymmetric gravity field. Nature 2018(555):220–222. https://doi.org/10.1038/nature25776

Iess L, Militzer B, Kaspi Y, Nicholson P, Durante D, Racioppa P, Anabtawi A, Galanti E, Hubbard W, Mariani MJ, Tortora P (2019) Measurement and implications of Saturn's gravity field and ring mass. Science 364:2965–2979. https://doi.org/10.1126/science.aat2965

Jacobson RA, Haw RJ, McElrath TP, Antreasian PG (2000) A comprehensive orbit reconstruction for the Galileo Prime mission in the J2000 system. J Astronaut Sci 48:495–516. https://doi.org/10.1007/BF03546268

James PB (2016) Geophysical constraints on Europa's ice shell and rocky core from a Flyby mission. In: Lunar and planetary science conference, vol 1903, p 2513.

Jia X, Kivelson MG, Khurana KK, Kurth WS (2018) Evidence of a plume on Europa from Galileo magnetic and plasma wave signatures. Nat Astron 2:459–464. https://doi.org/10.1038/s41550-018-0450-z

Kaula WM (1966) Theory of satellite geodesy. Blaisdell, Waltham (republished by, Dover, New York, 2000)

Khurana KK, Kivelson MG, Stevenson DJ, Schubert G, Russell CT, Walker RJ, Polanskey C (1998) Induced magnetic fields as evidence for subsurface oceans in Europa and Callisto. Nature 395:777–780. https://doi.org/10.1038/27394

Khurana KK, Kivelson MG, Russell CT (2002) Searching for liquid water in Europa by using surface observatories. Astrobiology 2:93–103. https://doi.org/10.1089/153110702753621376

Kivelson MG, Khurana KK, Joy S, Russell CT, Southwood DJ, Walker RJ, Polanskey C (1997) Europa's magnetic signature: report from Galileo's pass on 19 December 1996. Science 276(5316):1239–1241. https://doi.org/10.1126/science.276.5316.1239

Kivelson MG, Khurana KK, Stevenson DJ, Bennett L, Joy S, Russell CT et al (1999) Europa and Callisto: induced or intrinsic fields in a periodically varying plasma environment. J Geophys Res Space Phys 104(A3):4609–4625. https://doi.org/10.1029/1998JA900095

Kivelson MG, Khurana KK, Russell CT, Volwerk M, Walker RJ, Zimmer C (2000) Galileo magnetometer measurements: a stronger case for a subsurface ocean at Europa. Science 289(5483):1340–1343. https://doi.org/10.1126/science.289.5483.1340

Kliore AJ, Hinson DP, Flasar FM, Nagy AF, Cravens TE (1997) The ionosphere of Europa from Galileo radio occultations. Science 277:355–359. https://doi.org/10.1126/science.277.5324.355

Kliore AJ, Anderson JD, Armstrong JW, Asmar SW, Hamilton CL, Rappaport NJ, Wahlquist HD, Ambrosini R, Flasar FM, French RG, Iess L (2004) Cassini radio science. Space Sci Rev 115:1–70. https://doi.org/10.1007/1-4020-3874-7_1

Koh Z-W, Nimmo F, Lunine JI, Mazarico E, Dombard AJ (2022) Assessing the detectability of Europa's seafloor topography from Europa Clipper's gravity data. Planet Sci J 3:197. https://doi.org/10.3847/PSJ/ac82aa

Konopliv AS, Yoder CF, Standish EM, Yuan D-N, Sjogren WL (2006) A global solution for the Mars static and seasonal gravity, Mars orientation, Phobos and Deimos masses, and Mars ephemeris. Icarus 182(1):23–50. https://doi.org/10.1016/j.icarus.2005.12.025

Konopliv AS, Asmar S, Bills BG, Mastrodemos N, Park RS, Raymond CA, Smith DE, Zuber MT (2011) The Dawn gravity investigation at Vesta and Ceres. Space Sci Rev 163.1–4:461–486. https://doi.org/10.1007/s11214-011-9794-8

Konopliv AS, Park RS, Yuan DN, Asmar SW, Watkins MM, Williams JG, Fahnestock E, Kruizinga G, Paik M, Strekalov D, Harvey N (2013) The JPL lunar gravity field to spherical harmonic degree 660 from the GRAIL Primary mission. J Geophys Res, Planets 118(7):1415–1434. https://doi.org/10.1002/jgre.20097

Konopliv AS, Asmar SW, Park RS, Bills BG, Centinello F, Chamberlin AB, Ermakov A, Gaskell RW, Rambaux N, Raymond CA, Russell CT (2014) The Vesta gravity field, spin pole and rotation period, landmark positions, and ephemeris from the Dawn tracking and optical data. Icarus 240:103–117. https://doi.org/10.1016/j.icarus.2013.09.005

Konopliv AS, Park RS, Folkner WM (2016) An improved JPL Mars gravity field and orientation from Mars orbiter and lander tracking data. Icarus 274:253–260. https://doi.org/10.1016/j.icarus.2016.02.052

Konopliv AS, Park RS, Vaughan AT, Bills BG, Asmar SW, Ermakov AI, Rambaux N, Raymond CA, Castillo-Rogez JC, Russell CT, Smith DE (2018) The Ceres gravity field, spin pole, rotation period and orbit from the Dawn radiometric tracking and optical data. Icarus 299:411–429. https://doi.org/10.1016/j.icarus.2017.08.005

Kuskov OL, Kronrod VA (2005) Internal structure of Europa and Callisto. Icarus 177(2):550–569. https://doi.org/10.1016/j.icarus.2005.04.014

Lainey V, Karatekin Ö, Desmars J, Charnoz S, Arlot JE, Emelyanov N, Le Poncin-Lafitte C, Mathis S, Remus F, Tobie G, Zahn JP (2012) Strong tidal dissipation in Saturn and constraints on Enceladus thermal state from astrometry. Astrophys J 752(1):14. https://doi.org/10.1088/0004-637X/752/1/14

Lainey V, Jacobson RA, Tajeddine R, Cooper NJ, Murray C, Robert V, Tobie G, Guillot T, Mathis S, Remus F, Desmars J (2017) New constraints on Saturn's interior from Cassini astrometric data. Icarus 281:286–296. https://doi.org/10.1016/j.icarus.2016.07.014

Lainey V, Casajus LG, Fuller J, Zannoni M, Tortora P, Cooper N, Murray C, Modenini D, Park RS, Robert V, Zhang Q (2020) Resonance locking in giant planets indicated by the rapid orbital expansion of Titan. Nat Astron 4:1053–1058. https://doi.org/10.1038/s41550-020-1120-5

Lanyi GE, Roth T (1988) A comparison of mapped and measured total ionospheric electron content using global positioning system and beacon satellite observations. Radio Sci 23(4):483–492. https://doi.org/10.1029/RS023i004p00483

Lauf J, Calhoun M, Diener W, Gonzalez J, Kirk A, Kuhnle P, Tucker B, Kirby C, Tjoelker R (2005) Clocks and timing in the NASA deep space network. In: Proceedings of the 37th annual precise time and time interval systems and applications meeting. https://doi.org/10.1109/FREQ.2005.1574041

Lemoine FG, Smith DE, Zuber MT, Neumann GA, Rowlands DD (1997) A 70th degree lunar gravity model (GLGM-2) from Clementine and other tracking data. J Geophys Res, Planets 102(E7):16339–16359. https://doi.org/10.1029/97JE01418

Lemoine FG, Goossens S, Sabaka TJ, Nicholas JB, Mazarico E, Rowlands DD, Loomis BD, Chinn DS, Caprette DS, Neumann GA, Smith DE (2013) High–degree gravity models from GRAIL primary mission data. J Geophys Res, Planets 118(8):1676–1698. https://doi.org/10.1002/jgre.20118.

Leonard JM, Geeraert JL, Page BR, French AS, Antreasian PG, Adam CD, Wibben DR, Moreau MC, Lauretta DS (2019) OSIRIS-REx orbit determination performance during the navigation campaign. In: AAS/AIAA astrodynamics specialist conference, Portland, Maine, USA. AAS paper 19-714

Lesage E, Massol H, Schmidt F (2020) Cryomagma ascent on Europa. Icarus 335:11336. https://doi.org/10.1016/j.icarus.2019.07.003

Li Z, Ziebart M, Bhattarai S, Harrison D, Grey S (2018) Fast solar radiation pressure modelling with ray tracing and multiple reflections. Adv Space Res 61(9):2352–2365. https://doi.org/10.1016/j.asr.2018.02.019

Magnanini A, Fayolle M, Gomez Casajus L, Zannoni M, Tortora P, Lainey V, Dirkx D, Gurvits L, Mazarico E, Park R (2022) Combining JUICE and Europa Clipper range, range-rate and VLBI observables to improve the Galilean moons ephemerides. In: EGU general assembly 2022, EGU22-7836. https://doi.org/10.5194/egusphere-egu22-7836.

Marshall JA, Luthcke SB (1994) Modeling radiation forces acting on TOPEX/Poseidon for precision orbit determination. J Spacecr Rockets 31(1):99–105. https://doi.org/10.2514/3.26408

Mazarico E, Zuber MT, Lemoine FG, Smith DE (2009) Effects of self-shadowing on nonconservative force modeling for Mars-orbiting spacecraft. J Spacecr Rockets 46(3):662–669. https://doi.org/10.2514/1.41679

Mazarico E, Barker MK, Neumann GA, Zuber MT, Smith DE (2014) Detection of the lunar body tide by the Lunar Orbiter Laser Altimeter. Geophys Res Lett 41(7):2282–2288. https://doi.org/10.1002/2013GL059085

Mazarico E, Neumann GA, Barker MK, Goossens S, Smith DE, Zuber MT (2018) Orbit determination of the Lunar Reconnaissance Orbiter: status after seven years. Planet Space Sci 162:2–19. https://doi.org/10.1016/j.pss.2017.10.004

McGrath MA, Sparks WB (2017) Galileo ionosphere profile coincident with repeat plume detection location at Europa. Res Notes Am Astron Soc 1:14. https://doi.org/10.3847/2515-5172/aa988e

McGrath MA, Lellouch E, Strobel DF, Feldman PD, Johnson RE (2004) Satellite atmospheres. In: Bagenal, Dowling, McKinnon (eds) Jupiter. Cambridge University Press, Cambridge, pp 457–483

McGrath MA, Hansen CJ, Hendrix AR (2009) Observations of Europa's tenuous atmosphere. In: Pappalardo, McKinnon, Khurana (eds) Europa. University of Arizona Press, Tucson, pp 485–505

McKenzie D, Nimmo F (1997) Elastic thickness estimates for Venus from line of sight accelerations. Icarus 130(1):198–216. https://doi.org/10.1006/icar.1997.5770

McKinnon WB (2015) Effect of Enceladus's rapid synchronous spin on interpretation of Cassini gravity. Geophys Res Lett 42:2137–2143. https://doi.org/10.1002/2015GL063384

McKinnon WB, Zolensky ME (2003) Sulfate content of Europa's ocean and shell: evolutionary considerations and geological and astrobiological implications. Astrobiology 3:879–897. https://doi.org/10.1089/153110703322736150

Meltzer M (2007) Mission to Jupiter: a history of the Galileo project. National Aeronautics and Space Administration History Division NASA, Washington, SP-2007-4231

Melwani Daswani M, Vance SD, Mayne MJ, Glein C (2021) A metamorphic origin for Europa's ocean. Geophys Res Lett. https://doi.org/10.1002/essoar.10507048.1

Moirano A, Gomez Casajus L, Zannoni M, Durante D, Tortora P (2021) Morphology of the Io plasma torus from Juno radio occultations. J Geophys Res Space Phys 126:e2021JA029190. https://doi.org/10.1029/2021JA029190

Montenbruck O, Gill E (2000) Satellite Orbits. Springer, Berlin. https://doi.org/10.1007/978-3-642-58351-3

Moore WB, Schubert G (2000) The tidal response of Europa. Icarus 147:317–319. https://doi.org/10.1006/icar.2000.6460

Moyer TD (2000) Formulation for observed and computed values of Deep Space Network (DSN) data types. In: JPL publication 00-07, Jet Propulsion Laboratory, Pasadena, California

Murray CD, Dermott SF (1999) Solar system dynamics. Cambridge University Press, Cambridge

Nimmo F, Pappalardo RT, Giese B (2003) On the origins of band topography, Europa. Icarus 166(1):21–32. https://doi.org/10.1016/j.icarus.2003.08.002

Nimmo F, Thomas PC, Pappalardo RT, Moore WB (2007) The global shape of Europa: constraints on lateral shell thickness variations. Icarus 191(1):183–192. https://doi.org/10.1016/j.icarus.2007.04.021

O'Dea A, Kinman P (2019) Doppler tracking, DSN telecommunications link design handbook. Jet Propulsion Laboratory, 810-005. https://deepspace.jpl.nasa.gov/dsndocs/810-005/station-data-processing/

Ojakangas GW, Stevenson DJ (1986) Episodic volcanism of tidally heated satellites with application to Io. Icarus 66(2):341–358

Ojakangas GW, Stevenson DJ (1989) Thermal state of an ice shell on Europa. Icarus 81(2):220–241. https://doi.org/10.1016/0019-1035(89)90052-3

Paganini L, Villanueva GL, Roth L, Mandell AM, Hurford TA, Retherford KD, Mumma MJ (2019) A measurement of water vapour amid a largely quiescent environment on Europa. Nat Astron 4(3):266–272. https://doi.org/10.1038/s41550-019-0933-6

Paik M, Asmar SW (2010) Detecting high dynamics signals from open-loop radio science investigations. Proc IEEE 99(5):881–888. https://doi.org/10.1109/JPROC.2010.2084550

Palguta J, Anderson JD, Schubert G, Moore WB (2006) Mass anomalies on Ganymede. Icarus 180:428–441. https://doi.org/10.1016/j.icarus.2005.08.020

Palguta J, Schubert G, Zhang K, Anderson JD (2009) Constraints on the location, magnitude, and dimensions of Ganymede's mass anomalies. Icarus 201:615–625. https://doi.org/10.1016/j.icarus.2009.02.004

Pappalardo RT, Barr AC (2004) The origin of domes on Europa: the role of thermally induced compositional diapirism. Geophys Res Lett 31:L01701. https://doi.org/10.1029/2003GL019202

Pappalardo RT, McKinnon WB, Khurana K (eds) (2009) Europa University of Arizona Press, Tucson. https://uapress.arizona.edu/book/europa

Park RS, Asmar SW, Buffington BB, Bills BG, Campagnola S, Chodas PW, Folkner WM, Konopliv AS, Petropoulos AE (2011) Detecting tides and gravity at Europa from multiple close flybys. Geophys Res Lett 38:L24202. https://doi.org/10.1029/2011GL049842.

Park RS, Bills BG, Buffington BB, Folkner WM, Konopliv AS, Martin-Mur TJ, Mastrodemos N, McElrath TP, Riedel JE, Watkins MM (2015) Improved detection of tides at Europa with radiometric and optical tracking during flybys. Planet Space Sci 112:10–14. https://doi.org/10.1016/j.pss.2015.04.005.

Park RS, Riedel JE, Ermakov AI, Roa J, Castillo-Rogez J, Davies AG, McEwen AS, Watkins MM (2020) Advanced Pointing Imaging Camera (APIC) for planetary science and mission opportunities. Planet Space Sci 194:105095. https://doi.org/10.1016/j.pss.2020.105095

Pauer M, Musiol S, Breuer D (2010) Gravity signals on Europa from silicate shell density variations. J Geophys Res, Planets 115:E12005. https://doi.org/10.1029/2010JE003595

Pavlis DE, Nicholas JB (2017) GEODYN II System Description (Vols. 1–5), Contractor Report, SGT Inc. NASA, Greenbelt. https://space-geodesy.nasa.gov/techniques/tools/GEODYN/GEODYN.html

Perry ME, Neumann GA, Phillips RJ, Barnouin OS, Ernst CM, Kahan DS, Solomon SC, Zuber MT, Smith DE, Hauck SA, Peale SJ (2015) The low-degree shape of Mercury. Geophys Res Lett 42(71):6951–6958. https://doi.org/10.1002/2015GL065101

Petit G, Luzum B (2010) IERS conventions (2010). Bureau International des Poids et mesures, Sèvres

Phinney RA, Anderson DL (1968) On the radio occultation method for studying planetary atmospheres. J Geophys Res 73:1819–1827. https://doi.org/10.1029/JA073i005p01819

Phipps PH, Withers P (2017) Radio occultations of the Io plasma torus by Juno are feasible. J Geophys Res 122:1731–1750. https://doi.org/10.1002/2016JA023447

Phipps PH, Withers P, Buccino DR, Yang YM (2018) Distribution of plasma in the Io plasma torus as seen by radio occultation during Juno Perijove 1. J Geophys Res 123:6207–6222. https://doi.org/10.1029/2017JA025113

Phipps PH, Withers P, Buccino DR, Yang YM, Parisi M (2019) Variations in the density distribution of the Io plasma torus as seen by radio occultations on Juno Perijoves 3, 6, and 8. J Geophys Res Space Phys 124(7):5200–5221. https://doi.org/10.1029/2018JA026297

Phipps PH, Withers P, Vogt MF, Buccino DR, Yang YM, Parisi M, Ranquist D, Kollmann P, Bolton S (2020) Where is the Io plasma torus? A comparison of observations by Juno radio occultations to predictions from Jovian magnetic field models. J Geophys Res 125:e2019JA027633. https://doi.org/10.1029/2019JA027633

Rhoden A, Militzer B, Huff E, Hurford T, Manga M, Richards M (2010) Constraints on Europa's rotational dynamics from modeling of tidally-driven fractures. Icarus 210:770–784. https://doi.org/10.1016/j.icarus.2010.07.018

Roberts JH, Vance S, Ganse A (2018) Detection of gravity anomalies on Europa using line-of-sight gravity profiles. In: AGU fall mtg abstract PB42B-06

Rogstad S (2020) Open-loop radio science. In: DSN Telecommunications Link Design Handbook, JPL, 810-005. https://deepspace.jpl.nasa.gov/dsndocs/810-005/station-data-processing/

Roth L, Saur J, Retherford KD, Strobel DF, Feldman PD, McGrath MA, Nimmo F (2014) Transient water vapor at Europa's South pole. Science 343:171–175. https://doi.org/10.1126/science.1247051

Saur J, Strobel DF, Neubauer FM (1998) Interaction of the Jovian magnetosphere with Europa: constraints on the neutral atmosphere. J Geophys Res 103:19,947–19,962. https://doi.org/10.1029/97JE03556

Saur J, Neubauer FM, Glassmeier KH (2010) Induced magnetic fields in solar system bodies. Space Sci Rev 152:391–421. https://doi.org/10.1007/s11214-009-9581-y

Schenk PM (2020) The search for Europa's plumes: no surface patterns or changes 1979–2007? Astrophys J Lett 892:L12. https://doi.org/10.3847/2041-8213/ab6f78

Schilling N, Khurana KK, Kivelson MG (2004) Limits on an intrinsic dipole moment in Europa. J Geophys Res 109:E05006. https://doi.org/10.1029/2003JE002166

Schilling N, Neubauer FM, Saur J (2007) Time-varying interaction of Europa with the Jovian magnetosphere: constraints on the conductivity of Europa's subsurface ocean. Icarus 192:41–55. https://doi.org/10.1016/j.icarus.2007.06.024

Schinder PJ, Flasar FM, Marouf EA, French RG, Anabtawi A, Barbinis E, Kliore AJ (2015) A numerical technique for two-way radio occultations by oblate axisymmetric atmospheres with zonal winds. Radio Sci 50(7):712–727. https://doi.org/10.1002/2015RS005690

Schmidt BE, Blankenship DD, Patterson GW, Schenk PM (2011) Active formation of 'chaos terrain' over shallow subsurface water on Europa. Nature 479(7374):502–505. https://doi.org/10.1038/nature10608

Schubert G, Anderson JD, Spohn T, McKinnon WB (2004) Interior composition, structure and dynamics of the Galilean satellites. In: Bagenal F, Dowling TE, McKinnon WB (eds) Jupiter-the planet, satellites and magnetosphere. Cambridge University Press, Cambridge, pp 281–306

Schubert G, Sohl FG, Hussmann HF (2009) The interior of Europa. In: Pappalardo RT, McKinnon WB, Khurana KK (eds) Europa. University of Arizona Press, Tucson, pp 353–368

Sessa AM, Dombard AJ (2013) Gravity is the key experiment to address the habitability of the ocean in Jupiter's moon Europa. In: Fall mtg. Amer. Geophys. Union, Abst. P54A-10

Sloan ED, Koh CA (2008) Clathrate hydrates, 3rd edn. CRC Press, Boca Raton

Solomon SC, Bills BG, Margot J-L, Mazarico E, McKinnon WB, Nimmo F, Park RS, Roberts JH, Smith DE, Watkins MM, Zuber MT (2016) Report of the Gravity science working group for the Europa multiple flyby mission. Technical Report, National Aeronautics and Space Agency

Sotin C, Tobie G, Wahr J, McKinnon WB, McKinnon WB, Khurana KK (2009) Tides and tidal heating on Europa. In: Pappalardo RT, McKinnon WB, Khurana K (eds) Europa. University of Arizona Press, Tucson. https://uapress.arizona.edu/book/europa

Sparks WB, Schmidt BE, McGrath MA, Hand KP, Spencer JR, Cracraft M, Deustua SE (2017) Active cryo-volcanism on Europa? Astrophys J Lett 839:18. https://doi.org/10.3847/2041-8213/aa67f8

Srinivasan D, Sheldon C, Bray M (2017) Telecommunications systems for the NASA Europa missions. In: IEEE MTT-S international microwave symposium (IMS), pp 394–397

Steinbrügge G, Stark A, Hussmann H, Sohl F, Oberst J (2015) Measuring tidal deformations by laser altimetry. A performance model for the Ganymede Laser Altimeter. Planet Space Sci 117:184–191. https://doi.org/10.1016/j.pss.2015.06.013.

Steinbrügge G, Schroeder DM, Haynes MS, Hussmann H, Grima C, Blankenship DD (2018) Assessing the potential for measuring Europa's tidal Love number h_2 using radar sounder and topographic imager data. Earth Planet Sci Lett 482:334–341. https://doi.org/10.1016/j.epsl.2017.11.028

Steinbrügge G, Voigt JRC, Schroeder DM, Stark A, Haynes MS, Scanlan KM, Hamilton CW, Young DA, Hussmann H, Grima C, Blankenship DD (2020) The surface roughness of Europa derived from Galileo stereo images. Icarus 343:113669. https://doi.org/10.1016/j.icarus.2020.113669

Steinbrügge G, Hussmann H, Tobie G, Castillo-Rogez J, Lainey V, Stark A (2023) Tidal deformation and tidal evolution of Ganymede. In: Volverk M, McGrath M, Jia X, Spohn T (eds) Ganymede. Cambridge University Press, Cambridge. https://www.cambridge.org/core/books/ganymede/E6DFE8147262DB762C97C55DC7633ABC

Tamburo P, Withers P, Moore L, Dalba PA, Koskinen T (2019) Reanalysis of Cassini radio occultation data and electron density profiles for Saturn. In: Fall AGU meeting, abstract #P13B-3509

Tapley BD et al (2004) Statistical Orbit Determination. Academic Press, San Diego. https://doi.org/10.1016/B978-0-12-683630-1.X5019-X

Thor RN, Kallenbach R, Christensen UR, Gläser P, Stark A, Steinbrügge G, Oberst J (2021) Determination of the lunar body tide from global laser altimetry data. J Geod 95(1):1–14. https://doi.org/10.1007/s00190-020-01455-8

Tortora P, Zannoni M, Hemingway D, Nimmo F, Jacobson RA, Iess L, Parisi M (2016) Rhea gravity field and interior modeling from Cassini data analysis. Icarus 264:264–273. https://doi.org/10.1016/j.icarus.2015.09.022

US Geological Survey (2002) Controlled photomosaic map of Europa, Je 15M CMN. In: U.S. geological survey geologic investigations series I–2757, Flagstaff, AZ. http://pubs.usgs.gov/imap/i2757

Van Hoolst T, Rambaux N, Karatekin O, Dehant V, Rivoldini A (2008) The librations, shape, and icy shell of Europa. Icarus 195:386–399. https://doi.org/10.1016/j.icarus.2007.12.011

Van Hoolst T, Baland RM, Trinh A (2013) On the librations and tides of large icy satellites. Icarus 226(1):299–315. https://doi.org/10.1016/j.icarus.2013.05.036

van Noort B, Goossens S, Mazarico E, van der Wal W, Visser PN (2020) Titan gravity and tides from Cassini tracking data. In: American Geophysical Union, fall meeting 2020 abstract #P072-07

Vance SD, Roberts JH, Ganse AA (2015) Inverse theory for planning gravity investigations of icy moons. Lunar Planet Sci Conf 46:2751

Verma AK, Margot JL (2018) Expected precision of Europa Clipper gravity measurements. Icarus 314:35–49. https://doi.org/10.1016/j.icarus.2018.05.018

Wahr JM, Zuber MT, Smith DE, Lunine JI (2006) Tides on Europa, and the thickness of Europa's icy shell. J Geophys Res, Planets 111(E12):E12005. https://doi.org/10.1029/2006JE002729

Ward WR (1975) Tidal friction and generalized Cassini's laws in the solar system. Astron J 80:64–70. https://doi.org/10.1086/111714

Wieczorek MA (2007) Gravity and topography of the terrestrial planets. In: Planets and moons, treatise geophys, vol 10. Elsevier, Boston, pp 165–206. https://doi.org/10.1016/B978-044452748-6/00156-5

Withers P (2010) Prediction of uncertainties in atmospheric properties measured by radio occultation experiments. Adv Space Res 46:58–73. https://doi.org/10.1016/j.asr.2010.03.004

Withers P, Felici M, Mendillo M, Moore L, Narvaez C, Vogt MF, Oudrhiri K, Kahan D, Jakosky BM (2020) The MAVEN Radio Occultation Science Experiment (ROSE). Space Sci Rev 216:61. https://doi.org/10.1007/s11214-020-00687-6

Yakovlev OI (2002) Space radio science. Taylor & Francis, New York

Zannoni M, Hemingway D, Gomez Casajus L, Tortora P (2020) The gravity field and interior structure of Dione. Icarus 345:113713. https://doi.org/10.1016/j.icarus.2020.113713

Ziebart M (2001) High precision analytical solar radiation pressure modelling for GNSS spacecraft. PhD dissertation, University of East London

Zolotov MY, Kargel JS (2009) On the chemical composition of Europa's icy shell, ocean, and underlying rocks. In: Pappalardo RT, McKinnon WB, Khurana KK (eds) Europa. University of Arizona Press, Tucson, pp 431–457

Authors and Affiliations

Erwan Mazarico[1] · **Dustin Buccino[2]** · **Julie Castillo-Rogez[2]** · **Andrew J. Dombard[3]** · **Antonio Genova[4]** · **Hauke Hussmann[5]** · **Walter S. Kiefer[6]** · **Jonathan I. Lunine[7]** · **William B. McKinnon[8]** · **Francis Nimmo[9]** · **Ryan S. Park[2]** · **James H. Roberts[10]** · **Dipak K. Srinivasan[10]** · **Gregor Steinbrügge[2]** · **Paolo Tortora[11]** · **Paul Withers[12]**

✉ E. Mazarico
erwan.m.mazarico@nasa.gov

[1] NASA Goddard Space Flight Center, Greenbelt, USA

[2] NASA Jet Propulsion Laboratory, California Institute of Technology, Pasadena, USA

[3] University of Illinois Chicago, Chicago, USA

[4] Sapienza University of Rome, Rome, Italy

[5] German Aerospace Center, Cologne, Germany

[6] Lunar and Planetary Institute/USRA, Houston, USA

[7] Cornell University, Ithaca, USA

[8] Washington University in St. Louis, Saint Louis, USA

[9] University of California Santa Cruz, Santa Cruz, USA

10   Applied Physics Laboratory, Johns Hopkins University, Laurel, USA

11   University of Bologna, Bologna, Italy

12   Boston University, Boston, USA